Lawrence Berkeley National Laboratory
Recent Work

Title
PION-PION INTERACTIONS FROM n-p COLLISIONS AT 3 AND 4 BeV/c

Permalink
https://escholarship.org/uc/item/4cn0h97p

Author
Noble, Carl M.

Publication Date
1966-03-03

University of California

Ernest O. Lawrence Radiation Laboratory

PION-PION INTERACTIONS FROM π^-p COLLISIONS AT 3 AND 4 BeV/c

Berkeley, California

DISCLAIMER

UNIVERSITY OF CALIFORNIA

Lawrence Radiation Laboratory
Berkeley, California

AEC Contract No. W-7405-eng-48

PION-PION INTERACTIONS FROM π^-p COLLISIONS AT 3 AND 4 BeV/c

Carl M. Noble, Jr.

(Ph. D. Thesis)

March 3, 1966

PION-PION INTERACTIONS FROM π^-p COLLISIONS AT 3 AND 4 BeV/c

Contents

PION-PION INTERACTIONS FROM π^-p COLLISIONS AT 3 AND 4 BeV/c

Carl M. Noble, Jr.

Lawrence Radiation Laboratory
University of California
Berkeley, California

March 3, 1966

ABSTRACT

The final state π-π interaction in the process $\pi^- + p \rightarrow \pi^+ + \pi^- + n$ has been studied at incident momenta of 3 and 4 BeV/c by means of a magnetic spectrometer and spark chambers. A lead-sandwich counter system surrounding part of the hydrogen target rejected events of higher multiplicity to enhance detection of the $\pi^+\pi^-$n final state. The system, biased for low four-momentum transfer (Δ^2) acceptance, recorded 879 and 1248 $\Delta^2 < 9 \ \mu^2$ events at 3 and 4 BeV/c, respectively. The energy of the ρ peak in the dipion mass spectrum depends on Δ^2, $\theta_{\pi\pi}$ (the π-π scattering angle), and ϕ_{TY} (the Treiman-Yang angle). This dependence indicates that processes other than one-pion exchange are important.

The absorptive theory (which includes an I = 0, J = 0 particle, the ϵ^0) as proposed by Durand and Chiu qualitatively explains the ρ decay distribution ($\cos \theta_{\pi\pi}$ vs ϕ_{TY}). Unfortunately the geometrical bias precludes quantitative comparison and the calculation of meaningful cross sections.

In the ρ region, the forward-to-backward π-π scattering ratio is ≈ 0.5 for $\Delta^2 < 3 \ \mu^2$ and decreases with increasing Δ^2.

No direct evidence was seen for the $\omega \rightarrow 2\pi$ decay.

I. INTRODUCTION

A. Background Information on the Dipion Interaction

With few exceptions the data of the dipion interaction have been collected in bubble chambers and presented in the form of dipion mass plots which have shown substantial departures from phase space, particularly in the regions 750 and 1250 MeV.[1-7]

The bump at 750 MeV can be considered as a particle or resonance (called the ρ meson) and described by the usual quantum numbers: baryon number, strangeness, I spin, J spin, parity, and G parity. The baryon number is zero by the assumption of conservation of baryons.

The enhancement at 750 MeV has a large width. This is consistent with the hypothesis of the formation of a particle (the ρ) which decays rapidly (10^{-23} sec). Because of this, the decay pions are assumed to result from a strong interaction. Thus strangeness, I spin, J spin, P parity, and G parity are all assumed to be conserved. Hence the strangeness is zero.

Because the ρ decays into two pions, the I spin must be 0, 1, or 2. However, I = 0 and I = 2 are not possible because the ρ is seen in just three charge states. This leaves I = 1 as the only possibility. (Also the ρ has appeared in the reaction $p + p \rightarrow d + \rho^+$ in which the ρ^+ is in a pure I = 1 state.[8])

Because the two pions are bosons, the product of the spatial and isotopic wave functions must be symmetric. The I = 1 dipion isotopic wave function is antisymmetric because of the combination properties of the individual pion I-spin states. This makes the spatial wave function antisymmetric, which in turn means that the orbital angular momentum of the two pions must be odd. The decay $\rho \rightarrow \pi^0 \pi^0$ requires a symmetric spatial wave function and is forbidden if $I_\rho = 1$. This decay has not been observed experimentally.

Because the pions are spinless, the J spin of the ρ and the orbital angular momentum of the two pions are the same; thus, the J spin is odd. And because parity is conserved in the (strong) decay, the ρ parity must be negative.

The J spin of the ρ has been determined by analyzing the decay angular distribution in the ρ center of mass under the assumption of a dominant peripheral one-pion-exchange mechanism (strongly suggested by the Δ^2 distributions discussed in Sec. IV).

If the J spin were greater than 1, this decay distribution would contain terms proportional to $\cos^4\theta_{\pi\pi}$ or higher powers. The coefficients of the $\cos^4\theta_{\pi\pi}$ and higher terms obtained experimentally are consistent with zero, and a $\cos^2\theta_{\pi\pi}$ term is dominant; hence the J spin of the ρ is 1.

The G parity of the ρ is positive because the (rapid) decay is into an even number of pions. For neutral particles in an eigenstate of G and I, the C parity is equal to $G(-1)^I$ and is negative for the ρ^0.

Even though the quantum numbers of the ρ seem well established, there are some difficulties not yet resolved. For example:

(a) The central value of the mass peak varies from 740 to 775 MeV for different experiments and in some appears to shift upward with increasing four-momentum transfer to the nucleon.

(b) The values of the width vary even more, ranging from 65 to 210 MeV (Ref. 7).

(c) Another and apparently more serious problem is that of the decay angular distribution. (See Fig. 1 for angle definitions.) In the $\rho^\pm$ c.m. system, the ρ^+ and ρ^- have (approximately) a $\cos^2\theta_{\pi\pi}$ angular distribution, but the pions from ρ^0 decay have a large forward-backward asymmetry.

These effects have been explained as interference phenomenona.[9] The lifetime of the ρ is so short that it often decays near the target particle in such a manner that the decay pions can interact with the target. This means that other processes (background) can interfere with the decay distribution. Interference with background, which can lead to the above-mentioned effects, is discussed in more detail in Sec. IV.

Experimentally the production of ρ's in πp collisions is very forward with little four-momentum (Δ^2) transferred to the proton. This indicates a large impact parameter or peripheral mechanism in which the incoming pion interacts in the pion cloud. A natural model for this is the one-pion exchange, or OPE.

With the aid of the Feynman graph for the OPE, shown in Fig. 2 for πp, we can predict the following:

1. The ρ production should be a rapidly decreasing function of Δ^2. The problem here is that the production is decreasing even more rapidly than that predicted by OPE.

2. The (aligned) ρ-decay distribution in its own rest system for $J = 1$ should be proportional to $\cos^2\theta$, where θ is the polar angle between the incoming
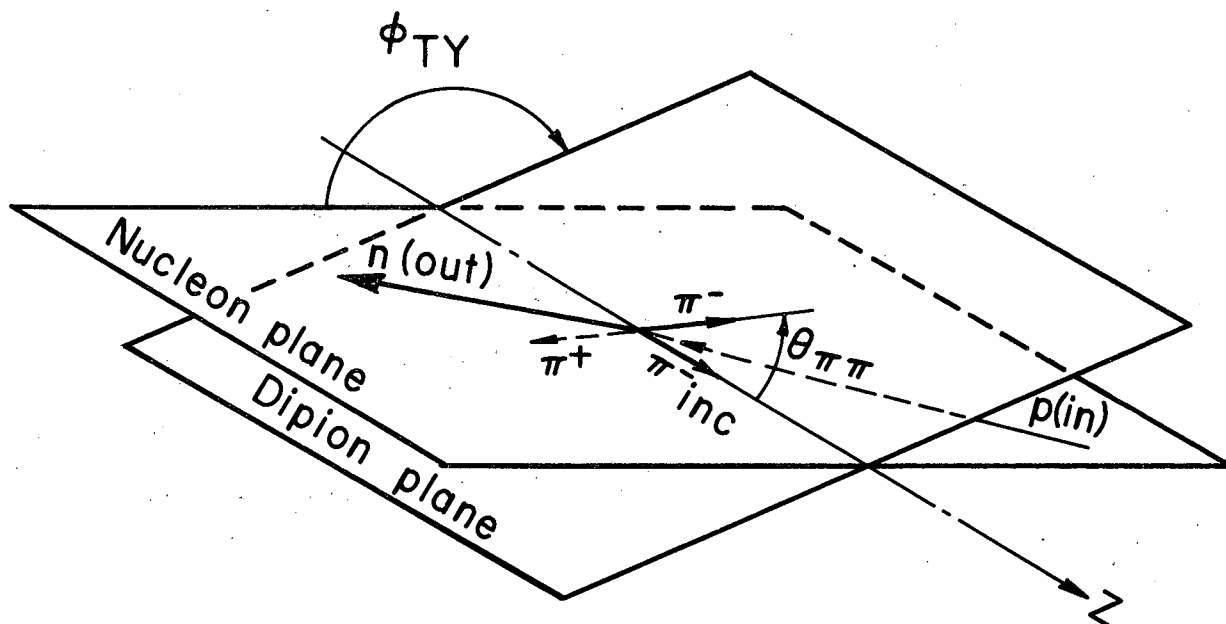
Fig. 1. Dipion c.m. system for fixed values of W, $M_{\pi\pi}$, and Δ^2
showing π-π scattering angle and Treiman-Yang angle (ϕ_{TY}).
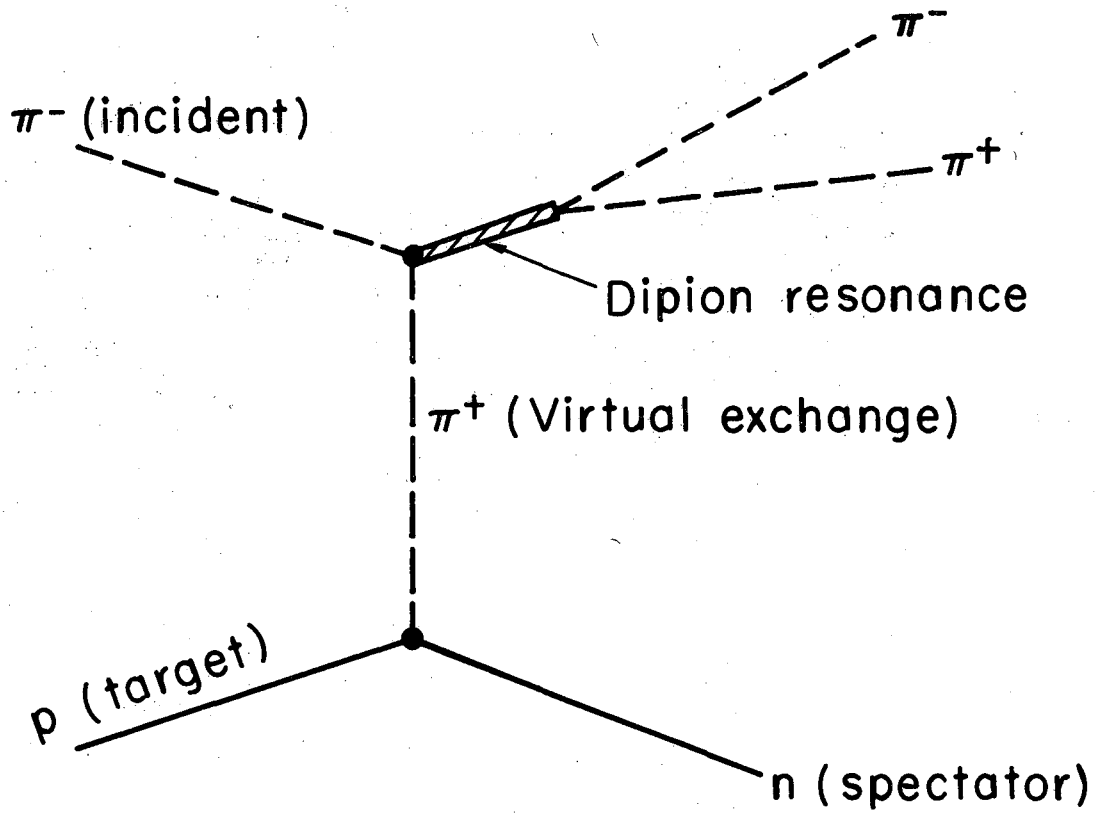
Fig. 2. One-pion-exchange (OPE) Feynman graph.

beam pion and outgoing pion with the same charge (the dipion scattering angle). Experimentally this proportionality does not hold for the neutral ρ, as was mentioned earlier.

3. The decay plane (formed by the beam pion and the decay pions) and the production plane (formed by the beam pion and the target particle) are connected by the exchanged pion which has $J = 0$. (Both planes are defined in the dipion c. m. system. See Fig. 1.) Thus, as Treiman and Yang[10] have pointed out, no angular information is transferred between the planes and there should be no angular correlation between them. This condition is satisfied at low Δ^2 for the charged ρ's, but the neutral ρ has a Treiman-Yang distribution that is not only anisotropic but strongly correlated with the dipion scattering angle, even at low Δ^2.

The difference in behavior between the neutral and charged states of the same particle is not now completely understood, although some explanations that have been given are consistent with the data.

Because the $\pi^+\pi^-$ state contains both $I = 0$ and $I = 1$, and the $\pi^-\pi^0$ or $\pi^+\pi^0$ state does not, it is natural to think that the cause of the anisotropy is an $I = 0$ dipion interaction that is coherent with the ρ production. Such an interaction could be resonant near the ρ mass and have a cross section much smaller than that of the ρ.

Other possible causes of anisotropy are $\omega \to 2\pi$ interference, isobaric effects, and absorption in the initial and final states. Of these, only the isobaric effects appear ruled out by the data; these will be discussed in more detail in Sec. IV.

The 1250-MeV enhancement, called the f^0, is thought to have the quantum numbers $IJ^{PGC} = 02^{+++}$ (see Ref. 4). These numbers have been established by techniques similar to those just described for the 750-MeV enhancement. The f^0 will not be discussed further here because the geometrical biases of this experiment strongly discriminated against dipion masses greater than 1 BeV.

B. Purpose

The purpose of this experiment was to examine in detail the neutral dipion final states in the low Δ^2 region ($\Delta^2 < 9\ \mu^2$) for $\pi^- + p \to \pi^+ + \pi^- + n$ with a large, high-resolution spark-chamber spectrometer system.

The physical aspects of the experiment are described in Sec. II, with a detailed account of the data analysis including the computer programs given in Sec. III.

The final two sections (IV and V) contain the results and conclusions, respectively.

II. EXPERIMENTAL SETUP

A. Introduction

The experiment was to measure the momenta and angles of the incident pion and final-state pions in the reaction $\pi^- + p \to \pi^+ + \pi^- +$ (missing mass).

The missing mass desired was a single neutron; events with larger missing mass (n + charged or neutral pions) were discriminated against by a lead-and-scintillator sandwich anticounter system surrounding part of the LH target.

Although part of the running time was devoted to π^+ and K^- incident beams, these data have not been analyzed carefully because so very few events were obtained.

B. Overall Physical Description

Figure 3 shows a plan view of the physical setup on the Bevatron floor. The beam design was a standard double-focus system with the first focus at the downstream end of Q_2 and the second at the H_2 target. The Čerenkov counters C_1 and C_2 were used in anticoincidence for K^- runs, but simply counted $\pi^\pm$'s otherwise.

The incident momenta and direction of a beam particle into the H_2 target were measured by the small-beam spark chambers a, β, γ, δ, L; the same quantities for the final-state pions were measured by the spectrometer system with spark chambers M, C, T, S, and A. The triggering logic is described in Sec. II. E.

Figures 4 and 5 are diagrams of the experimental layout and the individual spark-chamber design.

C. Beam Design

The beam optics were designed to maximize flux in a $\pm 3\%$ momentum region and direct it on the H_2 target of 5-in. diameter.

The beam pions were obtained by flipping a copper target [1/2-in. transverse by 1/4-in. high by 5 in. long (beam direction)] 17 mr upstream from the west straight section into the 6-BeV circulating proton beam of the Bevatron. The 4-BeV/c π^- at 0° and the 3-BeV/c π^- at 5° emerging from the thin window (Fig. 3) were bent by M_1. The quadrupole doublet Q_1 focussed the internal copper target at the downstream end of Q_2 where the beam was further restricted by
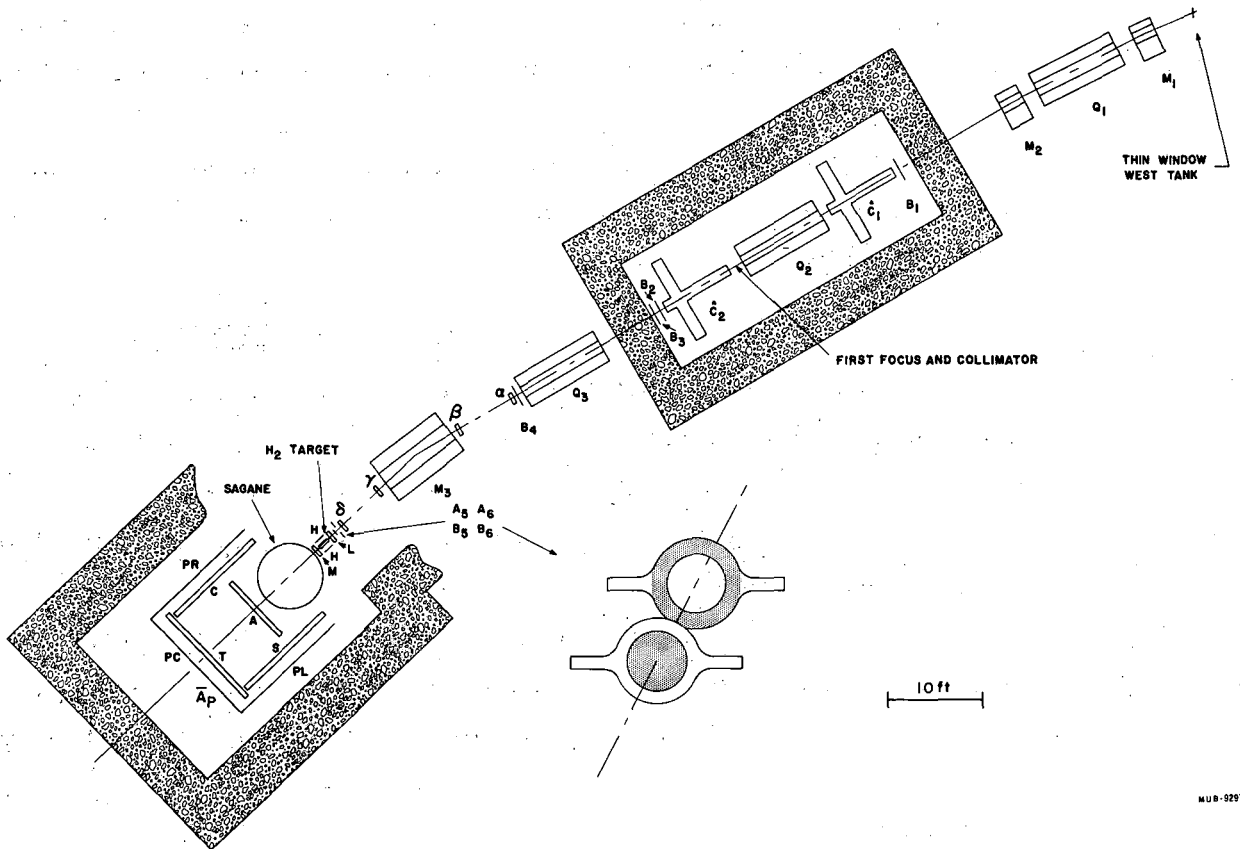
Fig. 3. Schematic layout on Bevatron floor.
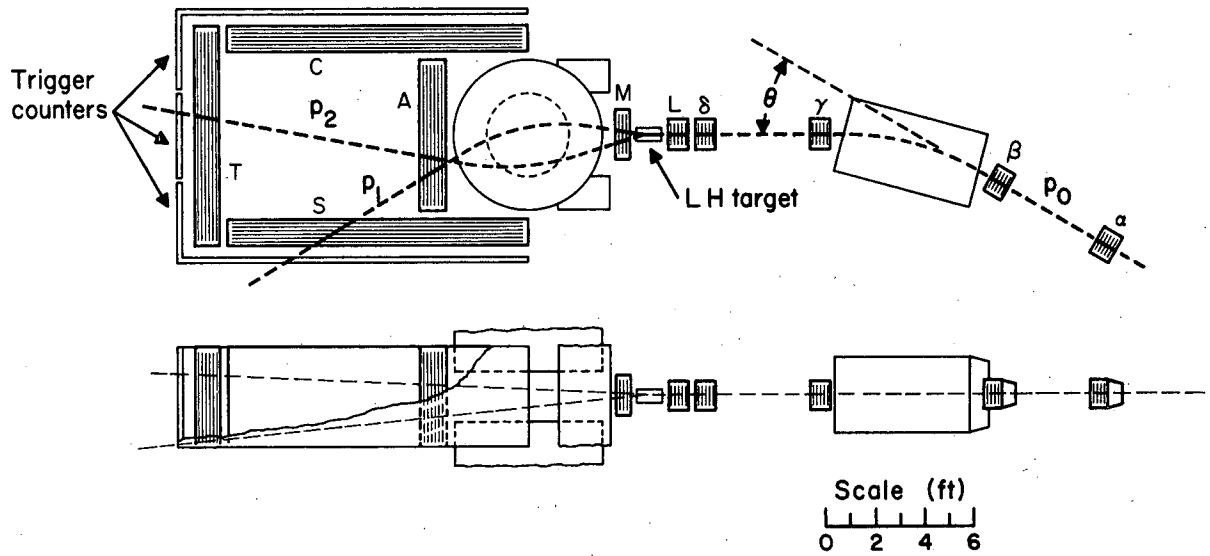
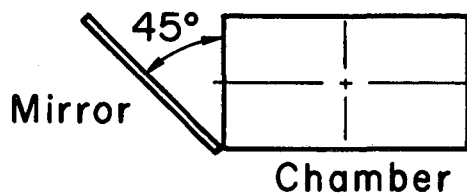Fig. 4.   Schematic layout emphasizing spark chamber positioning.

Effective camera

(a)

Fiducial grid

Chamber

Spark

7°

Mirror

Spark image

45°

Mirror

(b)
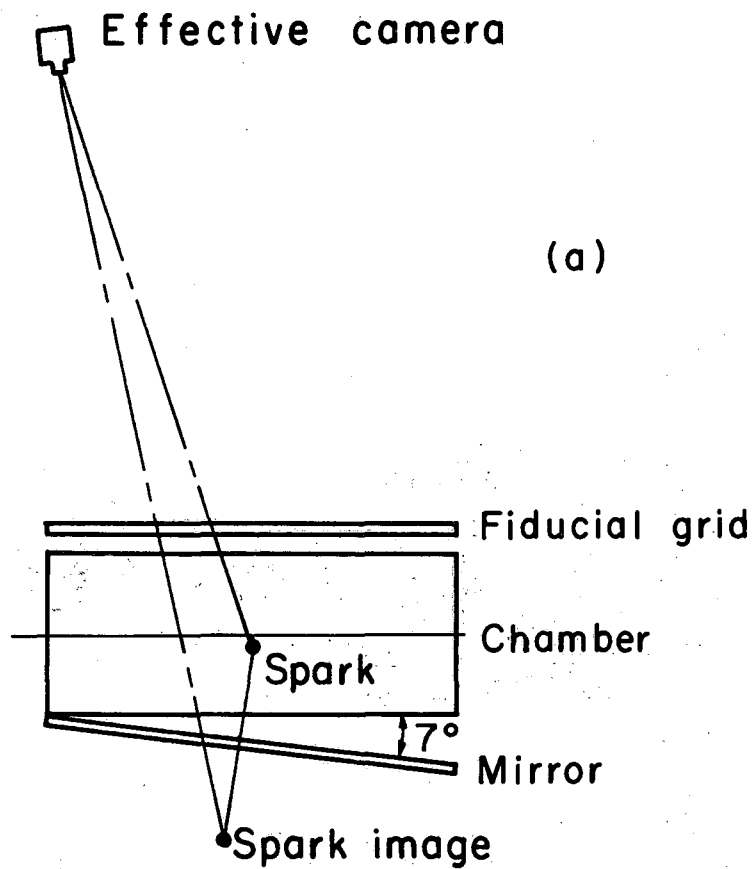
Chamber

MUB-9986

Fig. 5. Diagram of spark chambers showing stereo-mirror
positions. (a) C, T, S, A, and M all had the 7° mirror,
and (b) α, β, γ, δ, and L had the 45° mirror.

an adjustable brass collimator. Quadrupole Q_3 then focussed this inter-
mediate position onto the LH target. Finally, Q_2 acted like a field lens which
maximized the flux by imaging the exit aperture of Q_1 on the entrance aperture
of Q_3.

The horizontal bending magnet M_3, along with spark chambers α, β, γ,
δ, L, measured the incident momentum of the triggered event to $\approx 1/2\%$ and
the spatial position in the LH target to ≈ 1 mm.

Coulomb scattering was reduced by maintaining helium gas at atmos-
pheric pressure along the beam channel.

D. Apparatus

1. Target

As shown schematically in Fig. 6, the H_2 target flask was partly sur-
rounded by a lead-sandwich scintillation-counter system. These counters
vetoed higher multiplicity events, thereby enhancing the detection of the
$\pi^+\pi^-$n final state.

It was extremely important to cut down the number of unwanted trigger-
ings because the camera was dead for so long following triggering (film ad-
vance of ≈ 50 milliseconds). At an average beam rate of ≈ 70 π^- per milli-
second, a false triggering would waste ≈ 3500 beam particles. Also false
triggerings meant more pictures scanned unnecessarily.

The target flask was a cylinder 11 in. high and 5-in. in diameter, made
of 0.01 in. Mylar. The entrance and exit windows of the vacuum jacket were
0.040 in. aluminum, the minimum possible thickness consistent with safety
requirements.

2. Spark Chambers

The beam spark chambers (α, β, γ, δ) were small (5 by 9 in.) four-
gap chambers made of 0.002-in. aluminum foil sandwiched between 3/8-in.
Lucite "picture frames."[11]

The two ten-gap chambers (L, 5 by 5 in.; M, 10 by 24 in.) were of
similar construction.

The four chambers behind the magnet, each of which had four gaps
≈ 4 by 8-1/2 ft^2 in area, were made by bonding 0.003-in. aluminum foil to
aluminum frames. The four-gap assembly was suspended in a gas-tight box
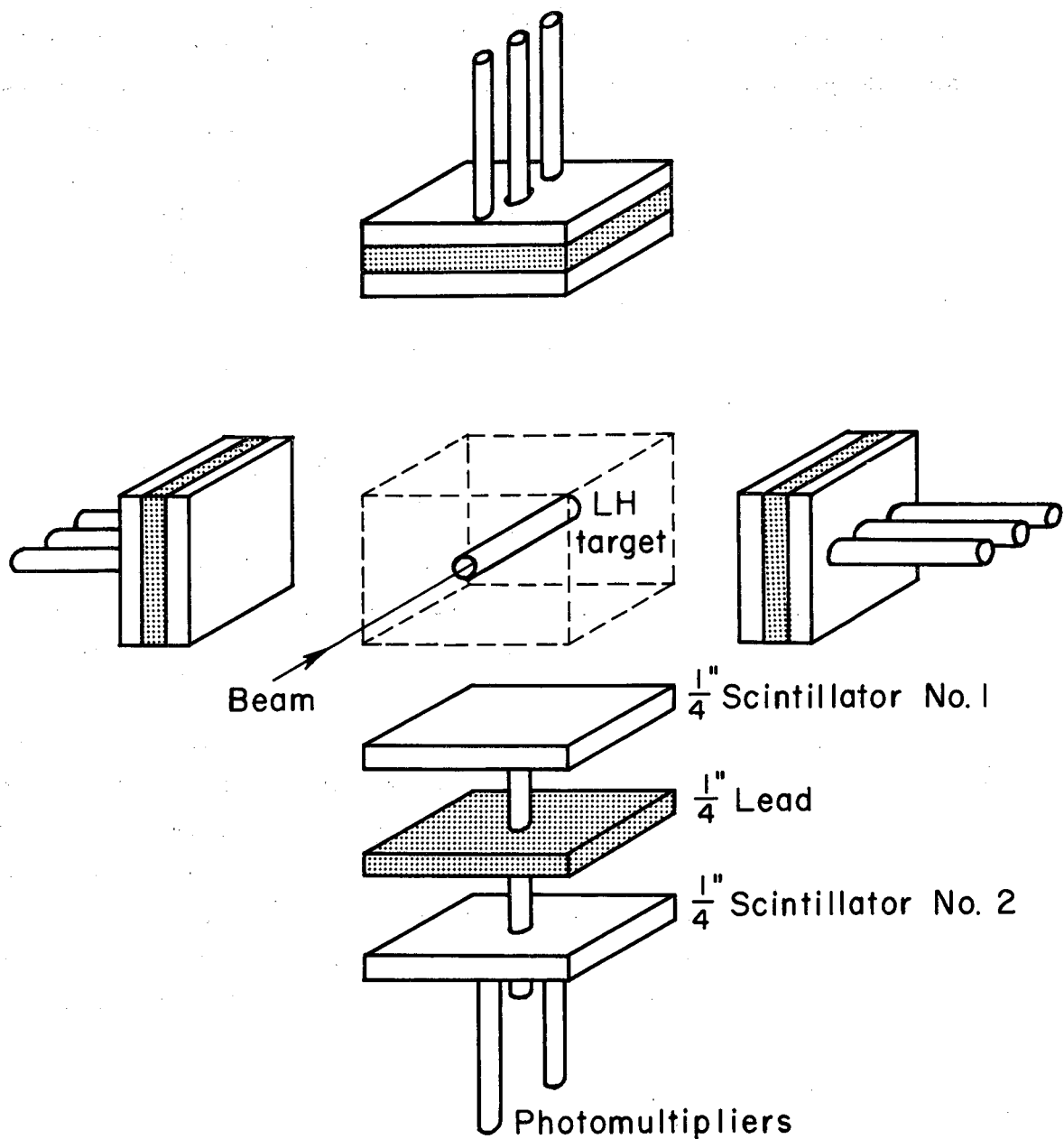whose sides were 0.007-in. Mylar.

Fig. 6. Exploded schematic view of lead-sandwich anticounters
surrounding LH target.

All chambers were continuously flushed with a mixture of 10% helium + 90% neon.

3. Fiducials

A set of grids with a single longitudinal scribe and transverse scribes every 4 in. (±1/6-in.) were suspended above each chamber. Each grid was edge-lighted by xenon flash tubes which flashed once each trigger.

4. Optics

A representation of the entire optical scheme, is shown in Fig. 7.

The beam chambers along with L had 45° mirrors mounted alongside each to provide the stereo view. Due to space limitations, the M, C, T, S, and A chambers provided stereo views by a mirror placed under each chamber at an angle of 7° with respect to the horizontal. The vertical coordinates were then only $\approx 1/5$ as accurate as the horizontal ones. Since these chambers were large, it was impractical to build the usual field lens for them, and the spatial reconstruction of tracks was thus much more complicated than usual.

5. High Voltage

All spark chambers were fired by a 15-kV pulse supplied by spark gaps. These spark gaps were triggered by a master gap that derived its pulse from a vacuum-tube amplifier using an EIMAC 4PR60A tetrode.

The 15-kV pulse came from a low-inductance capacitor bank that had been used in several previous experiments at the Bevatron. The special design[12] was necessary because efficient operation requires pulses of high energy (several joules) and low rise times.

6. Camera

The camera, a modified Flight Research Model 4C with a 37 to 50 msec film-advance time, used Dupont 140B film and a 108-mm lens with an exposure setting of f/8.

E. Electronics

The spark chambers were triggered only if all of the following criteria were satisfied (see Fig. 8 for the logic, and Fig. 3 for counter identification):

(a) A gate initiated by the Bevatron control signal was on.

(b) The camera was ready, i.e., the film was advanced.

No. 3   No. I

No. 2

Beam   L M   C,S

                                A   T

Camera

No. 3

                            5
        9
    11   4 7
    10   8   6
Beam α   β   γ   δ

                        Camera
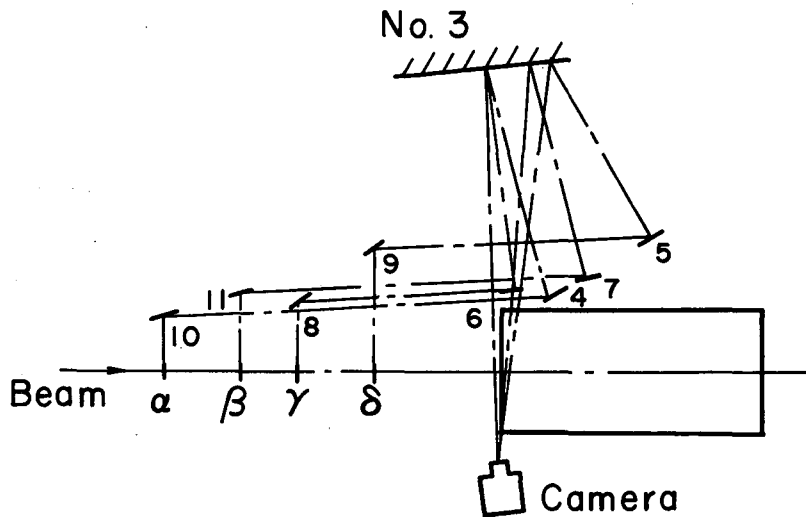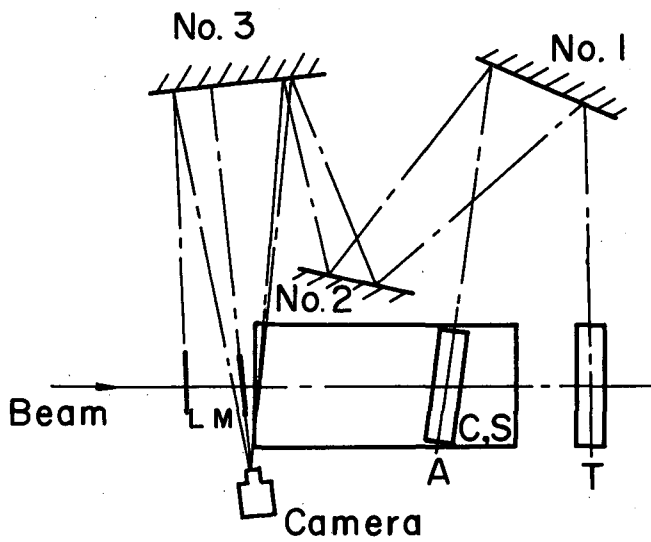
MUB-9863

Fig. 7. Optics. Above: L, M, C, T, S, and A optics. Below:
    beam chamber optics. Hachured numbered areas are mirrors.
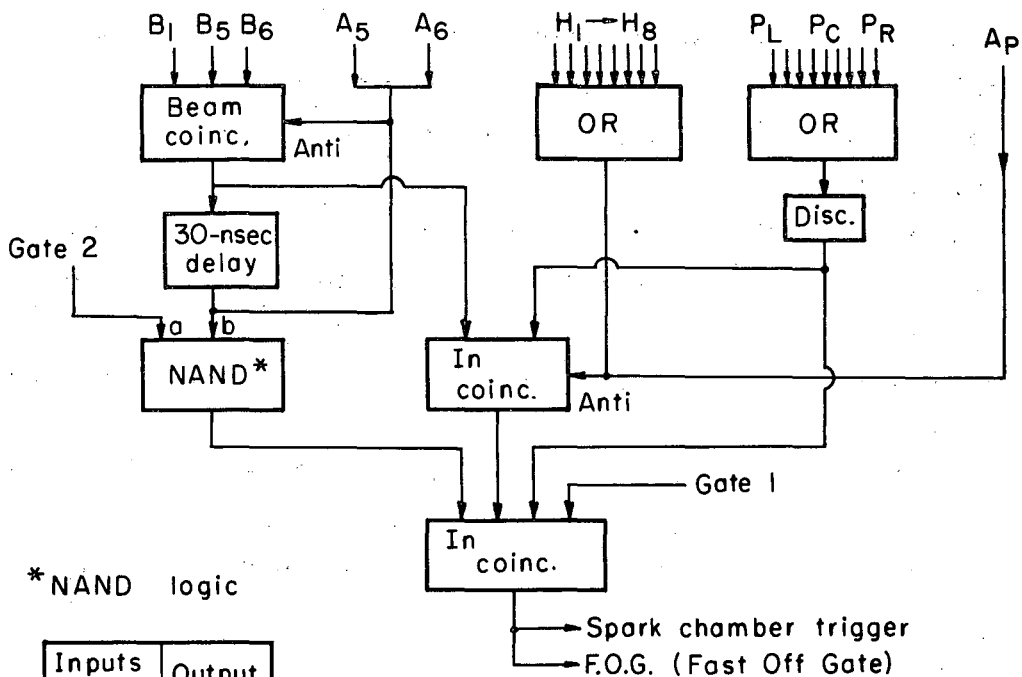
Inputs		Output
a	b	
O	O	O
I	O	I
O	I	O
I	I	O

*NAND logic

I = voltage present
O = no voltage present

MUB-9864

Fig. 8.   Simplified electronic logic of the triggering system.

(c) A beam particle had not traversed the system in the last one-half microsecond. (An 0.5-μsec pulse derived from the B_1, B_5, B_6 coincidence or $\overline{A}_5 \overline{A}_6$ anticoincidence turned off the I_n coincidence circuit.)

(d) A beam particle caused a pulse from B_1, B_5, and B_6, and none out of $\overline{A}_5 \overline{A}_6$, the guard anticounter that ensured a trajectory nearly parallel to the H_2 target.
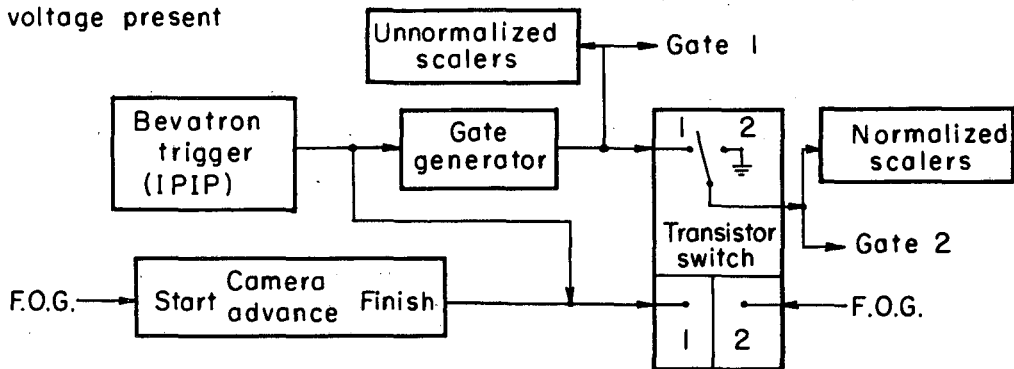
(e) No pulses came from $\overline{A}_p$, the beam anticounter, or the $\overline{H}_2$ lead-sandwich counters.

(f) Two pulses came from the peripheral counters P_L, P_R, and P_C.

The peripheral counters were all connected to a 50-channel adder-discriminator which limited, added, and discriminated the output.

F. Magnets

The magnets used in this experiment are described in Table I.

The Sagane magnet was modified to have a 23-in. gap. The return paths were arranged as shown in Fig. 9 so that the final-state particles would have no obstructions over as large a solid angle as possible. The horizontal acceptance of ±45° and the vertical acceptance of ±8° made the total solid angle (lab) subtended at the target 0.36 sr.

Table I. Description of magnets used in experimental setup.

Magnet	Dimensions and type (in.)	Power required (kW)
M_1, M_2	9×12 C	14
M_3	12×60 H	425
Sagane	40-in. diam circular	500
Q_1	8×32 doublet	40
Q_2	8×32 doublet	40
Q_3	8×32 doublet	40
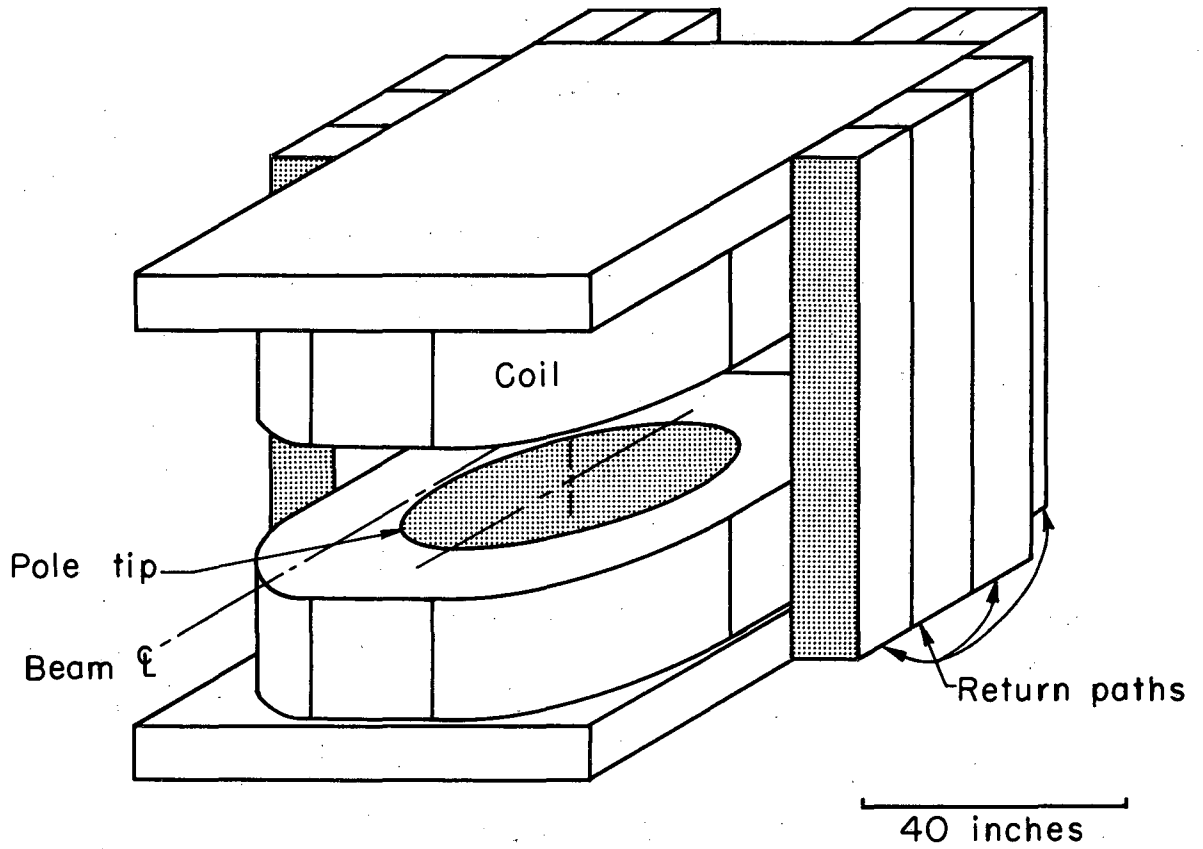
Fig. 9. Isomatric scale drawing of Sagane with 23-in. gap
magnet used in this experiment.

III. DATA ANALYSIS

A. Alignment

The four basic optical systems involved in getting all ten spark chambers on the same frame were:

  (a) Beam chambers α and β,

  (b) Beam chambers γ and δ,

  (c) The H_2 chambers L and M,

  (d) The big downstream chambers C, T, S, and A. (See Fig. 7.)

Each of these systems required separate mirrors for most of their optical paths, with the high mirror #3 being common to all. Thus it is important to know the relationships of the four systems with respect to the Sagane and M_3 magnets. Unfortunately, the mirrors in all of the systems moved significantly during the experiment and the analysis programs had to be fed fiducial corrections as a function of run number. (The run number appears on the film. Each run was no more than 2 hours long.) Apparently, the mirror movement was caused by temperature changes.

At momenta 2, 3, and 4 BeV/c, data were taken with the Sagane field up, down, and off (all with H_2 out of the target flask). The $\bar{A}_p$ counter was used in coincidence instead of the peripheral counters P_L, P_R, and P_C; these straight through data were used to align the system. Also it was possible to remove the beam chambers and photograph a light "floating" current-carrying wire that simulated the various beam momenta. By measuring these pictures on a digitized projector (SCAMP,[13] which is described in Sec. III. B), we could calibrate the beam momenta from the spark positions in the beam chambers.

The magnetic field of the Sagane magnet was mapped by a 1-in. flip coil with a digital voltmeter connected to an IBM card punch.[14] The magnetic-field component B_z, where the direction z is up, was measured in a 2-by-2-by-2-in. grid from the H_2 target to the A chamber. This encompassed a region 70 by 70 by 24 in. The horizontal components B_x and B_y were calculated by means of the Maxwell curl relation $\vec{\nabla} \times \vec{B} = \vec{0}$. This instrument was accurate to about 10 G; when measurement errors were ignored, it was possible to integrate an orbit numerically in three dimensions through this field so that the exit position was known to within 0.001 in. The idea here was to know the field well enough so that the orbit integration, which was involved

in the alignment and general event analysis, would contribute no significant error to each particle's trajectory.   This technique, together with the same computer programs, has been used successfully in other later experiments.

Systems (b), (c), and (d) were lined up with the Sagane-magnet-off "straight throughs." This lining up sounds trivial, but in practice was difficult because of the extremely high demagnification of 200.   The next step was to use the straight-throughs with the Sagane magnet on, and to check that the magnet performance and the beam results were the same as when the magnet was off.

A "typical" event is shown in Fig. 10, where the severity of the optical distortions is apparent in the nonlinearity of the grid lines.   These distortions had to be removed by the reconstruction computer program before any events could be completely processed.   The M, C, T, S, and A chambers each had strip mirrors underneath for providing stereo view; these mirrors distorted the reflected sparks even more.   The grid lines above each chamber were illuminated and the resulting reflected images were photographed in a test run.   The distortions due to the stereo mirrors were then calculated from these photographs, which were measured by SCAMP.

It was at this point that real events could be processed and physical quantities calculated.   At first the missing-mass spectrum, which shows a strong neutron peak, looked different for opposite directions of the Sagane-magnet field.   Measurements of the magnetic field were then made at several spatial positions for each polarity (the magnitude of the current being equal for the two polarities).   The absolute value of the field at each position did not depend upon the polarity.

Next, a larger sample of straight-through pictures was measured. Several troubles such as scanning biases in the original sample and a programming error in the momentum reconstruction showed up.

All in all, about five iterations of the entire procedure were necessary to find and remove the mistakes and align the system properly.

B.   Scanning and Measuring

1.   General Discussion

The events were both scanned and measured first on SCAMP I, [13] which projects the film onto a ground-glass screen; this screen rotates and is digitized with a smallest measured movement of 0.628 mr.   The film stage is
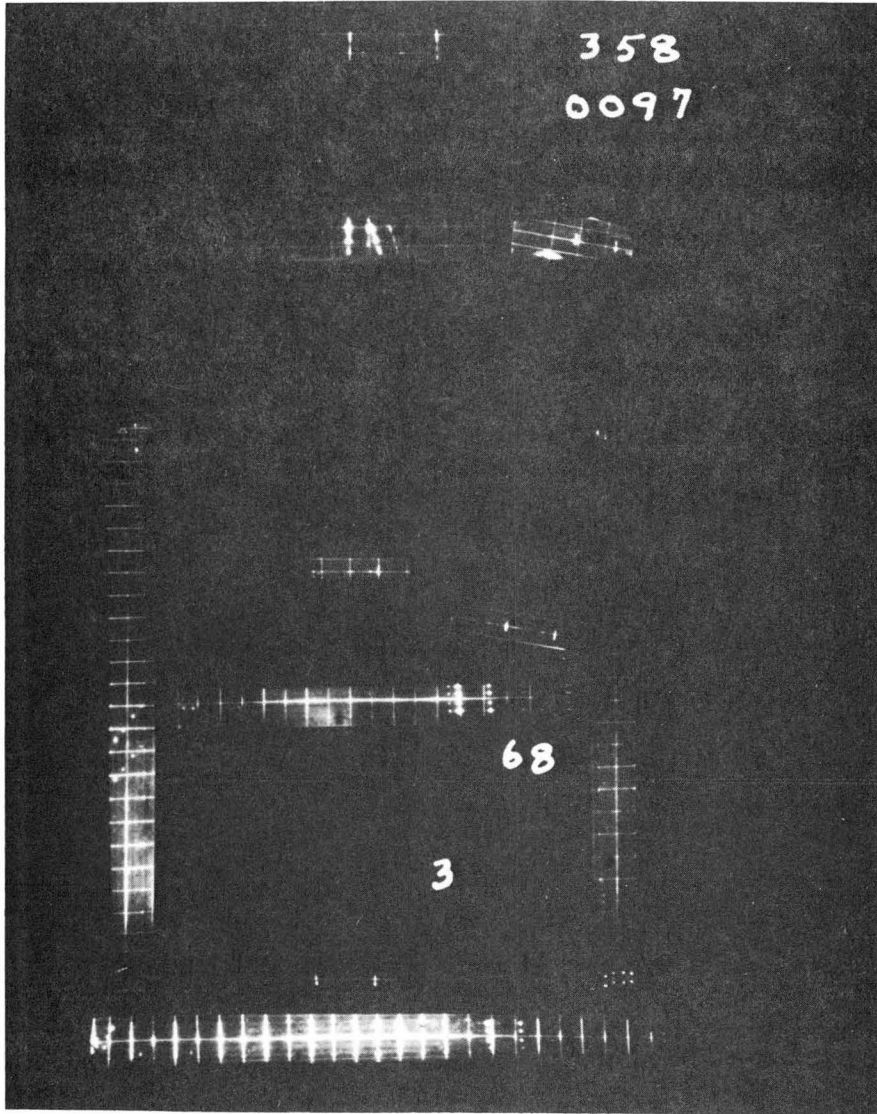
ZN-5460

Fig. 10. Photograph of a typical event. Note the optical distortions evidenced by crooked grid lines in the longer chambers (CTSA). Note also that for each particle trajectory in a given chamber, two sets of sparks are shown, one the actual and one the stereo image.

movable in two orthogonal directions with a smallest measured movement of 1 micron. The screen contains a single fiducial line marked along a diameter and a short perpendicular at the center of rotation. The x, y position of the stage and the angular position of the screen were punched on paper tape with certain constants and event codes set on a parameter board. As a later alternative, film was scanned without measurement and a list of detected events was made for the measurers. A much more consistent set of data resulted from this mode of operation.

2. Scanning Instructions

Most of the background (ratio 20 → 50:1) events contained only one trajectory in the M chamber, the trigger coming from scatterings and/or cosmic-ray accidentals. Thus a large number of background pictures could be discarded quickly after a glance at the M chamber. If there were two trajectories in M, than all of the following criteria had to be satisfied for an event to be measurable (see Fig. 4 for chamber positions):

(a) Only one trajectory must be in each beam chamber;

(b) Only two trajectories must be in the CTSA system;

(c) All CTSA tracks and images involved must have four sparks;

(d) If A contains a trajectory, a corresponding trajectory must appear downstream;

(e) If T contains a trajectory, A must contain the corresponding one.

If there was any doubt about its measurability, the event was measured. The philosophy behind the procedure was to have rather loose acceptance requirements for the measurers. The more-restrictive acceptance criteria were then written into the analysis computer programs. Measuring rules were applied to ensure that the measurers did not waste time on too many bad events.

3. Measuring

For each event, the measurer had five fiducial points plus a minimum of 9 and a maximum of 11 track-image pairs to measure. Since all the chambers were in a low-field or field-free region, the sparks appeared in a straight line. Thus, to save measuring time, the reticule line on the screen was positioned on top of all the sparks in a given chamber, so that the x-y coordinate of each spark did not have to be measured. The run, Bevatron

pulse, and frame numbers, along with a binary code designating the down-
stream (CTSA) chambers involved, were set on the parameter board and
punched on the paper tape.

Six thousand 4-BeV/c and five thousand 3-BeV/c events were measured
at the rate of 32 to 40 per 4-hour shift.

C. Analysis Program

The paper tape from SCAMP was processed first by an IBM 1401 com-
puter, which was programmed to make simple checks such as the number of
measurements, tape format, and parameter-board information; the rejected
events were listed for remeasurement; but the others were written on a
magnetic tape for input to the IBM 7044 or 7094.

I now describe the IBM 7094 programs for two-prong events. (Straight
throughs were analyzed by the same routines with omission of certain obvious
parts.)

These programs comprising about 12 000 machine language words of
order code and 17 000 storage words, mostly for the Sagane magnetic field,
were written specifically for this experiment along the lines of the FOG-
CLOUDY-FAIR[15] or PACKAGE[16] systems used for bubble-chamber analysis.
Of course the programs used in this dipion analysis are much more specific,
but the basic ideas are the same. Our programs were all written in FORTRAN
IV and run on the LRL-IBM MONITOR SYSTEM in four separate jobs described
next in outline form.

JOB #1 —

Inputs $\begin{bmatrix} 1. & \text{Tape with fiducial constants vs run number} \\ 2. & \text{1401 output tape} \end{bmatrix}$

(a) Fiducial check and transformation from SCAMP coordinates to film
coordinates.

(b) Calculation of intersection of tracks and images with principal grid
line for each chamber.

(c) Calculation of optical distortions (CTSA chambers only).

(d) Calculation of REAL SPACE coordinates of trajectory in each chamber
and associated weights on the basis of the relevant track-image pair.

(e) CTSA pattern recognition; calculation of position and angles of the two
downstream trajectories.

(f) Calculation of incident momentum from beam chambers.

(g) Output binary tape for input to JOB #2.

JOB #2 –

Inputs ⌈ 1.   Tape with magnetic-field values

⌊ 2.   JOB #1 output binary tape

(a) Matching each of the two M chamber trajectories with their downstream counterparts (CTSA). Since the field of the Sagane magnet is cylindrically symmetric to about 3%, this matching is conveniently done by comparing upstream (M) and downstream trajectory impact parameters with respect to the center of the Sagane magnet. (From the given chamber (e.g., M) construct a straight extension of the track, in the horizontal plane, of the trajectory through the Sagane magnet. The length of the perpendicular to this extension from the magnet's center is defined to be the impact parameter.)

(b) Calculation of the position and angles in M and momenta of the two final-state particles. This is accomplished for each trajectory by an iterative procedure involving an initial momentum approximation ($\pm 5\%$) from a formula

$$P = \frac{A(b^2)}{\Delta\theta} - bB(b^2) \, ,$$

where b is the upstream-downstream average-impact parameter, $A(b^2)$ and $B(b^2)$ are polynomials in b^2, and $\Delta\theta$ is the measured horizontal bending angle through the Sagane magnet. An orbit in numerically integrated from M through the Sagane magnet, and compared with the measured downstream position and impact parameter.[17] The vertical focusing can be estimated from this orbit's vertical deflection and an appropriate correction made at M. After correction of the horizontal angle and momentum from the formula, a second orbit is run and again comparisons are made. This is continued for a maximum of eight orbits until the difference between the downstream orbit position and the corresponding measured position is less than 0.01 in. in absolute value. This was between 1/5 and 1/7 the error in measurement of this quantity and thus could be ignored as a source of error in the final analyses.

(c) Output – binary tape for JOB #3.

JOB #3 –

Inputs ⌈ 1.   Tape with detection efficiencies

⌊ 2.   JOB #2 output tape

(a) Calculation of unconstrained physical quantities: missing mass, dipion mass, four-momentum transfer, scattering angle, Treiman-Yang angle, and isobar masses.

(b) Kinematical constraining: the missing mass was constrained along with a vertex location in the H_2 target for the following assumed event types:

$$\pi^- + p \rightarrow \pi^- + p \qquad (1)$$
$$\pi^- + p \rightarrow \pi^- + p + \pi^0 \qquad (2)$$
$$\pi^- + p \rightarrow \pi^+ + \pi^- + n \qquad (3)$$
$$\pi^- + p \rightarrow K^+ + K^- + n. \qquad (4)$$

Usual nonlinear iterative least-squares techniques were used in constraining.[18] The main difference between this constraining program and a bubble chamber program such as GUTS[19] is that our input variables were independent positions in space, corresponding to the chamber measurements rather than the usual correlated curvature, horizontal angle, and dip angle. Also, the vertex in the H_2 target was not measured directly but was inferred from the incoming and outgoing trajectories.

(c) Calculation of constrained quantities and their statistical errors.

(d) Output for JOB #4.

JOB #4 –

Inputs [1. Output from JOB #3

2. Cards describing CRT plots desired

(a) Calculation of CRT scatter plots for any two of the following variables (both constrained and unconstrained quantities may be plotted):

1. Dipion mass in BeV,

2. Dipion mass squared in BeV^2,

3. Δ^2 in pion-mass-squared units,

4. $\cos\theta_{\pi\pi}$,

5. Treiman-Yang angle in degrees,

6. Mass of $\pi^- n$ in BeV,

7. Mass of $\pi^+ n$ in BeV,

8. (Mass of $\pi^- n)^2$ in BeV^2,

9. (Mass of $\pi^+ n)^2$ in BeV^2.

(b) Calculation of vertical and horizontal scatter-plot projections (un-
weighted and weighted histograms).

This routine plots 1000 graphs in one-half hour on the 7094 Mark II.
Most of the histograms and scatter plots in this report are photographs from
this program's CRT film.

D. Bias Determination

1. Description of the Interaction

The reaction $\pi^- + p \to \pi^+ + \pi^- + n$ is kinematically defined by the follow-
ing five parameters (if the polarizations of the nucleons are not measured).

(a) W, the overall invariant center-of-mass energy, which is determined
by the incident pions' momentum.

(b) V or $M_{\pi\pi}$, the dipions' invariant mass.

(c) Δ^2 or t, the invariant four-momentum transfer to the nucleon, usually
measured in μ^2 (pion-mass squared) units and defined as positive in
the physical (space-like) region.

(d) $\cos\theta_{\pi\pi}$, with $\theta_{\pi\pi}$ the dipion scattering angle that is the polar angle
between the incoming and the outgoing π^-'s in the dipion c.m. system.

(e) ϕ_{TY}, the Treiman-Yang angle that is an azimuth about the incoming
π^- direction in the dipion c.m. system.

Figure 1 shows the momentum vectors and the defined parameters in
the dipion c.m. system for fixed values of W, V, and t.

The Treiman-Yang angle ranges from 0° to 360°. However, if parity
is conserved in the interaction and the polarizations of the nucleons are not
measured, all physical quantitites and distributions should be symmetric
about 180°. This can easily be seen by considering the "nucleon plane" in
Fig. 2 to be a mirror. Checks made to see if these distributions were
symmetric about 180° showed that the results were consistent with parity
conservation. (This was also a good check on the spatial-reconstruction
programs and the electronic-trigger system.)

Any other angle or mass such as the angle between the π^- and the n or
the invariant π^-n mass are functions of (a) through (e) and are not independent
quantities.

2. Individual-Event Efficiency

The final state of each event was defined by the momentum, horizontal angle, and dip angle for each trajectory in the laboratory at some point in the H_2 target. Consider the event rotated about the incident pion direction (in the lab) a full 360°. (There is no "physics" in the azimuthal distribution because the target protons are unpolarized and the incident particle has no spin.) Often for some of the rotated orientations, one or both of the final-state trajectories will not physically be able to reach the CTSA chambers due to the location of the magnet pole tips and return paths. The detection efficiency is then defined as the fraction of possible rotated events for which both final-state trajectories get through the Sagane magnet and reach the CTSA system.[20]

In order to avoid unnecessary orbit integrations as each event was analyzed, we ran a separate group of test orbits originating at the center of the H_2 target, with varying momenta and angles. From these orbits we obtained a two-parameter numerical function of momentum and polar angle with respect to the average beam direction. (The beam direction was constant to within $1/2°$.) This function set the limits of rotation of a given vector within the effective aperture of the system.

With this function it was possible to calculate by interpolation the range of permissible rotations of the individual vectors, and thus the detection efficiency.

3. Monte Carlo Technique

It is important to examine also the efficiency of the system from another viewpoint, i.e., given a fixed beam momentum, a region in dipion mass, four-momentum transfer, scattering angle, and Treiman-Yang angle, ask the question: How many of the events in this region will be detected by the system? The answer to this was obtained by generating events by a Monte Carlo technique similar to FAKE[21] and processing them as if they had originated at the center of the LH target.

Table II shows some sample efficiencies. Note that for low Δ^2 in the region of the ρ there are no events in which final-state particles go backward in the lab system, and that in only 6 to 8% a particle with momentum lower than 250 MeV/c exists. (Particles with momentum lower than this spiral and stop in the Sagane magnet and never reach the CTSA system.)

Table II. Sample efficiencies

	$M_{\pi\pi} \Delta^2$ in μ^2								
	700 to 740 MeV			800 to 840 MeV			1200 to 1240 MeV		
	$0 \to 3$	$3 \to 6$	$0 \to 25$	$0 \to 3$	$3 \to 6$	$0 \to 25$	$2 \to 6$	$6 \to 9$	$9 \to 25$
$\vec{p}_1$ or $\vec{p}_2$ backward in lab system	0	0	0	0	0	0	0.02	0.02	0.03
$|\vec{p}_1|$, $|\vec{p}_2| < 250$ MeV/c	0.06	0.06	0.07	0.08	0.08	0.09	0.09	0.09	0.09
Both detectable	0.33	0.3	0.21	0.28	0.25	0.19	0.16	0.15	0.10

Entries are probabilities determined by Monte-Carlo calculations. Here $\vec{p}_1$ and $\vec{p}_2$ are the final-state-pion vectors in the laboratory system.

Figure 11 shows the correlations induced by the system. The curves show lines of constant detection probability in the $\cos\theta_{\pi\pi}$ vs ϕ_{TY} plot for several $M_{\pi\pi}$ and Δ^2 regions. The highest detection probability is at the center of each plot and the lowest near the edges.

As long as Δ^2 is less than $25\,\mu^2$ and the dipion mass is near that of the ρ, only the edges near the corners are discriminated against severely. Hence the detection efficiency measured for each event is an excellent approximation to the true efficiency, except for large Δ^2 or V and for certain regions in the $\cos\theta_{\pi\pi}$ vs ϕ_{TY} plot. (Note that because of experimental symmetry a quantity like $\frac{F-B}{F+B}$, where F = events with $\cos\theta_{\pi\pi} > 0$ and B = events with $\cos\theta_{\pi\pi} < 0$, is not biased as long as symmetrical regions of Treiman-Yang angle are considered.)

4. Weighted Histograms and Scatter Plots

Consider a group of events "i" in a dipion mass interval which is represented by one bin in a histogram. Each ith event has an efficiency e_i for being detected, and a weight w_i which equals $1/e_i$. Let n $(=\Sigma i)$ be the normal or unweighted bin value, and let $\sigma(n)$ $(=\sqrt{n})$ be the statistical error. Then N equals Σw_i, the weighted bin value, and $\sigma(N)$ equals $(\Sigma w_i^2)^{1/2}$, the statistical error of the weighted bin value. (See Appendix for the justification.)

The approximate nature of the efficiency calculation gave for a few events a value near zero, which in the weighted histogram created a large bin that was unrealistic. Even though the statistical error was also large, the large bin gave a misleading appearance to the histogram. After analyzing a scatter plot of efficiency vs $M_{\pi\pi}$, I decided upon a minimum efficiency of 0.1 which involves few events in the ρ region. The computer was programmed to set the efficiency to 0.1 if the calculated value was lower.

In the same spirit, I made weighted scatter plots by the following prescription: The weight for each point of the unweighted scatter plot was rounded to the nearest integer (1 to 10). This rounded weight equals the number of points that are then plotted randomly in a rectangular region whose size is of the order of the average measurement error. For locations near a kinematic boundary, points are often plotted outside a physical limit, e.g., Fig. 15. This along with the problem of estimating the statistical errors makes the weighted plot of limited use. However, an ordinary scatter plot is also limited in that it is generally composed of points with widely varying
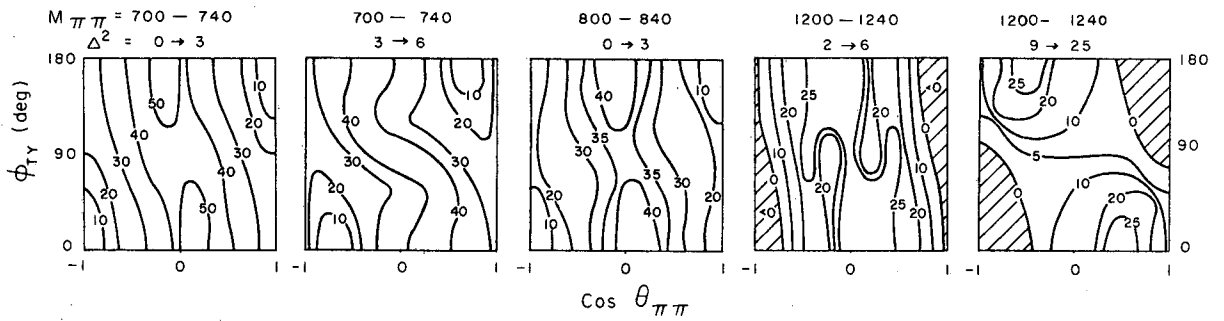
Fig. 11.   Approximate bias curves for 4 BeV/c.   The numbers
     are detection probabilities in percent.

precisions. In fact, numerical comparisons with theory are most often made by one-dimensional projections (such as histograms and ideograms).

In this report all weighted scatter plots will be preceded by the ordinary one so that the true quantity of data can readily be seen.

E. Selection of Events

In all of the analysis programs, the final-state charged particles are assumed to be pions. No attempt was made to determine this experimentally, but it can be shown that the background from non-dipion events was negligible. Other possible two-prong final states are:

1. $\pi^- + p$
2. $\pi^- + p + $ (one or more) π^0's
3. $K^+ + K^- + N$
4. $K^+ + K^- + N + $ (one or more) π^0's
5. $e^+ + e^- + N$
6. $\pi^+ + \pi^- + N + $ (one or more) π^0's
7. Associated production of strange particles.

The elastic scatters were not seen because of the necessarily large opening angle ($> 62°$) for final-state momenta greater than 250 MeV/c. Also, if mistakenly treated as a $\pi^+ \pi^-$ final state, the calculated dipion mass for such events was always greater than 1.1 BeV. In the constraining program we attempted to fit all events to the elastic criterion, but found none.

Event types 2, 4, and 6 all had at least one π^0 and thus were rejected to a large extent by the lead-sandwich counters. The constraining program, of course, reduced this background even further.

In the rest of this paper, the final-state charged particles are assumed to be pions unless stated otherwise in the text.

Figures 12(a) and (b) show the 3-BeV/c unconstrained missing-mass histograms, unweighted and weighted respectively. A comparison of the two shows the effect of the geometrical bias; the higher missing-mass values (greater than $\approx$ 1.1 BeV) being suppressed in the unweighted plot are clearly more prominant in the weighted one. The unconstrained missing mass of those events that satisfied the constraint criteria are shown in the weighted histogram of Fig. 12(c). These events are $\pi^+ \pi^- n$ final states with a small percentage (less than 5%) having an extra π^0. Because a smooth dipion mass spectrum (not shown) results from events with a missing mass of 1.08 BeV
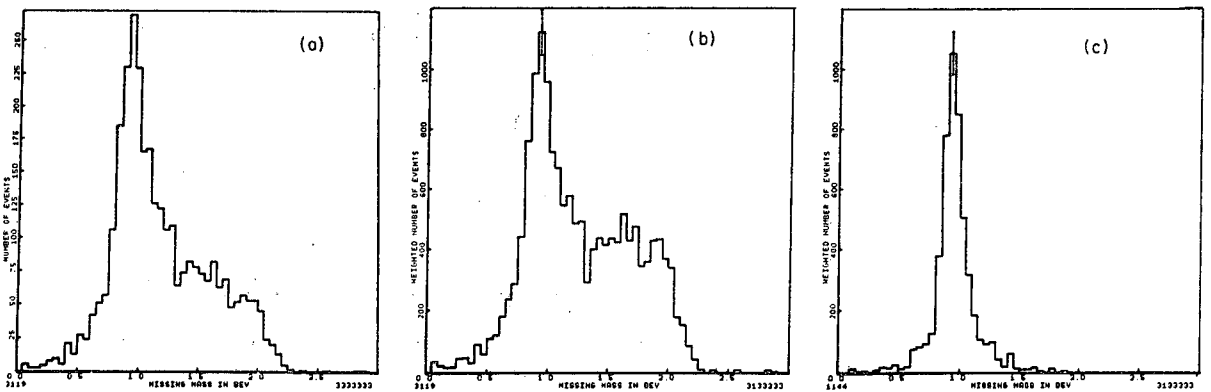
Fig. 12. 3-BeV/c missing-mass spectra:
    (a) Unweighted histogram; unconstrained.
    (b) Weighted histogram; unconstrained.
    (c) Weighted histogram; unconstrained values of events
        that passed the constraining criterion.
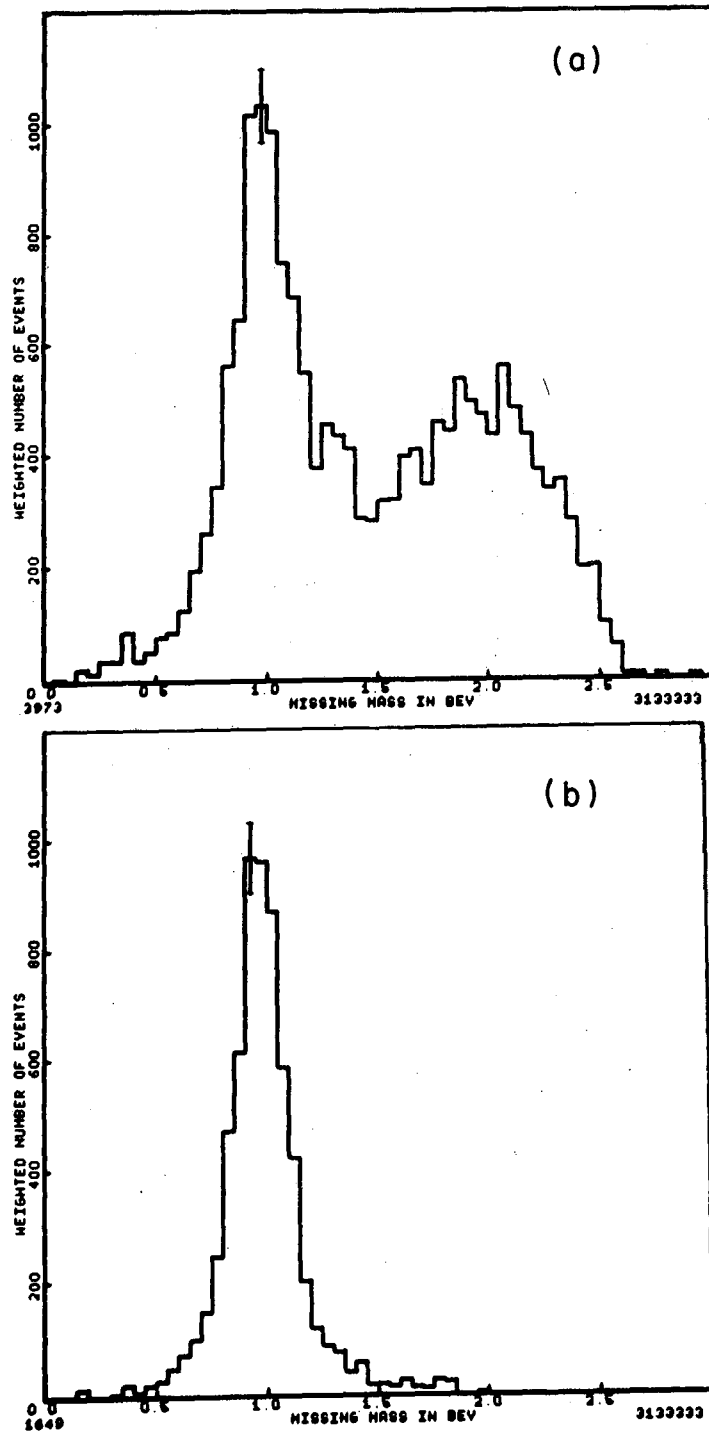
MUB-9974

Fig. 13. 4-BeV/c missing-mass spectra:
    (a) Weighted histogram; unconstrained.
    (b) Weighted histogram; unconstrained values of
        events that passed the constraining criterion.

or greater, all such events were treated as if they were $\pi^+\pi^-$ n final states.
Figures 13(a) and (b) are the 4-BeV/c weighted missing-mass spectra corre-
sponding to the 3-BeV/c spectra in Figs. 12(b) and (c), respectively.

Most of the events that satisfied the dipion constraining criteria also
fit hypothesis 3. However, the production $K\overline{K}$ cross section is small and a
plot of the $K\overline{K}$ mass spectrum is smooth. Also, it can be shown that if a
sharp $K\overline{K}$ resonance were formed and the final-state particles (K's) mistak-
enly identified as pions, the resulting dipion mass spectrum would be smooth.[22]
Small production cross sections also remove types 5 and 7 from consideration.

F. Accuracy

The optical distortions and the high demagnification reduced the potential
accuracy of this experiment. Some representative standard deviations are
listed in Table III. In some cases the constraining program reduced the
statistical errors by as much as a half, which led to the smallest histogram
bin choices of 20 MeV for dipion mass and 1 μ^2 for Δ^2. This is unimportant
here since the information content of this experiment is limited by the stat-
istics rather than the measurement accuracy.

G. Cross Sections

The geometrical bias precludes the calculation of accurate production
cross sections. Even a cross section for a limited region in Δ^2 involves a
large correction for certain regions of $\cos\theta_{\pi\pi}$ and ϕ_{TY}. Figure 11 illustrates
this.

The basic problem involved is as follows. Consider a region in $M_{\pi\pi}$,
Δ_2, $\cos\theta_{\pi\pi}$, and ϕ_{TY}. An event in this region falls into one of two categories:
  (a) The event is physically undetectable even if rotated about the beam axis
(e. g. , one of the final-state momenta is < 250 MeV/c).
  (b) The event is detectable with a probability (detection efficiency) deter-
mined by the limits of rotation about the beam axis. (See Sec. III. D.2.)
As long as the ratio of the number of type (a) events to type (b) is small for
events in the specified region, a meaningful cross section can be calculated.
However, even a small region on the Chew-Low (Δ^2, $M_{\pi\pi}$) plot involves
some domains in the $\cos\theta_{\pi\pi}$, ϕ_{TY} plot that have a large ratio of (a) to (b)
(in particular, around the periphery).

Table III. Measurement errors

Variable	Standard deviation
Horizontal position	0.06 in. = 7.5 μ on film
Vertical position	0.3 in.
γ-δ or A-T horizontal angle	1.4 mrad
M horizontal angle	9 mrad
C, T, S, or A angle	10 mrad
4 BeV/c straight through	80 MeV
3 BeV/c straight through	60 MeV
2 BeV/c straight through	40 MeV
Unconstrained $M_{\pi\pi}$ in ρ region	15 MeV
$M_{\pi\pi}$ in f region	25 MeV
Missing mass	120 MeV
Δ^2 in low Δ^2 region	0.5 μ^2

Unfortunately these domains are locations of considerable structure in the data. Although an estimate of the lost data certainly could be made, it would be of questionable value. Since the bubble-chamber cross-section measurements appear to be quite consistent and of approximately the same statistical content as this experiment, I decided not to attempt these estimates and so calculated no accurate cross sections. However I did check to make certain that the data rates were reasonable and consistent with the known cross sections.

IV. RESULTS

All data in the scatter plots and histograms described in the following sections have been constrained.

A. Mass Spectra

Figures 14(a) and (b) show the 3-BeV/c dipion mass spectra for low Δ^2 ($0 \to 9\,\mu^2$) and high Δ^2 ($9 \to 50\,\mu^2$); the corresponding spectra for 4 BeV/c follows in Fig. 14(c) and (d). The kinematical upper limit for Δ^2 is $\approx 200\,\mu^2$ at 3 BeV/c and $330\,\mu^2$ at 4 BeV/c, but the biases are such that only 3% of the data is above $50\,\mu^2$. The ρ stands out clearly at both energies and appears to shift upward ≈ 20 MeV, going from low to high Δ^2 (Ref. 23). There is also indication of the f^0 (≈ 1250 MeV) in the high Δ^2 data even though the biases against detection are severe.

Figure 15(a) shows a Chew-Low unweighted plot for a 3-BeV/c data and 15(b) a weighted plot. Similar plots for 4 BeV/c are shown in Figs. 16(a) and (b). (It is characteristic of these plots that some of the added points lie outside kinematic boundaries.) The concentration of events in the ρ region near the lower kinematic limit is characteristic of a dominant one-pion-exchange (OPE) mechanism.

Figures 17(a), (b), and (c) show the 3-BeV/c weighted dipion-mass spectra for the following Δ^2 ranges: $0 \to 3\,\mu^2$; $3 \to 6\,\mu^2$; $6 \to 9\,\mu^2$. The corresponding histograms for the 4-BeV/c data are shown in Figs. 18(a), (b), and (c), where a possibility of structure appears in the ρ region; however this is slightly less than a 2-standard-deviation effect. This will be pursued more fully later.

B. Isobars

Isobar effects are certainly small, especially at low Δ^2, as has been consistently noted in the literature for beam momenta over 2 BeV/c.[24] The Dalitz plots in Figs. 19 through 21 show no obvious isobaric effects; however, the geometrical bias does discriminate against points corresponding to dipion masses greater than 1 BeV. Hence the dominant "ρ band" makes the isobar effect hard to find even if it were present.
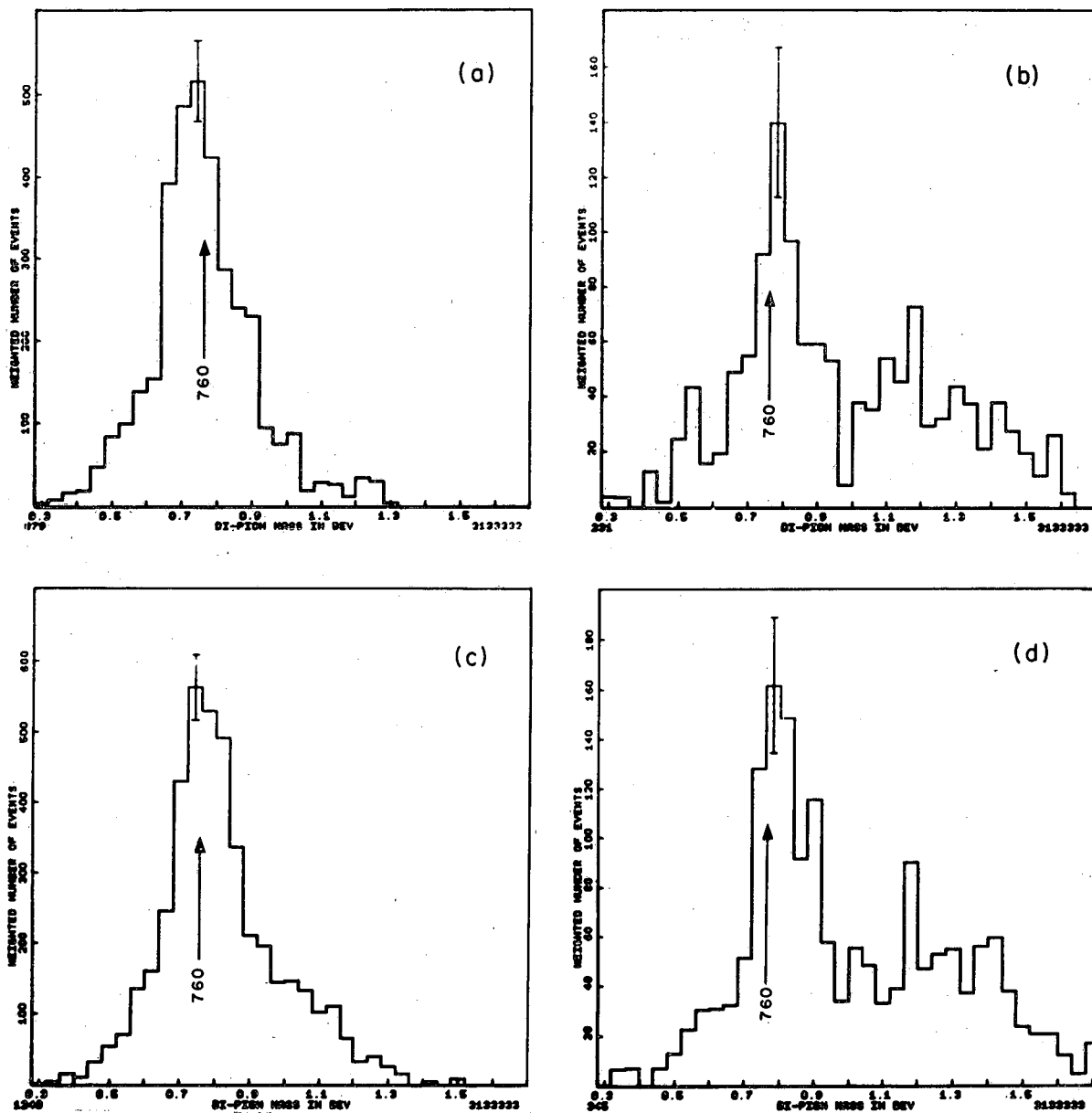
Fig. 14.   Dipion weighted histogram:
(a) 3 BeV/c $\Delta^2 < 9 \mu^2$
(b) 3 BeV/c $\Delta^2 > 9 \mu^2$
(c) 4 BeV/c $\Delta^2 < 9 \mu^2$
(d) 4 BeV/c $\Delta^2 > 9 \mu^2$
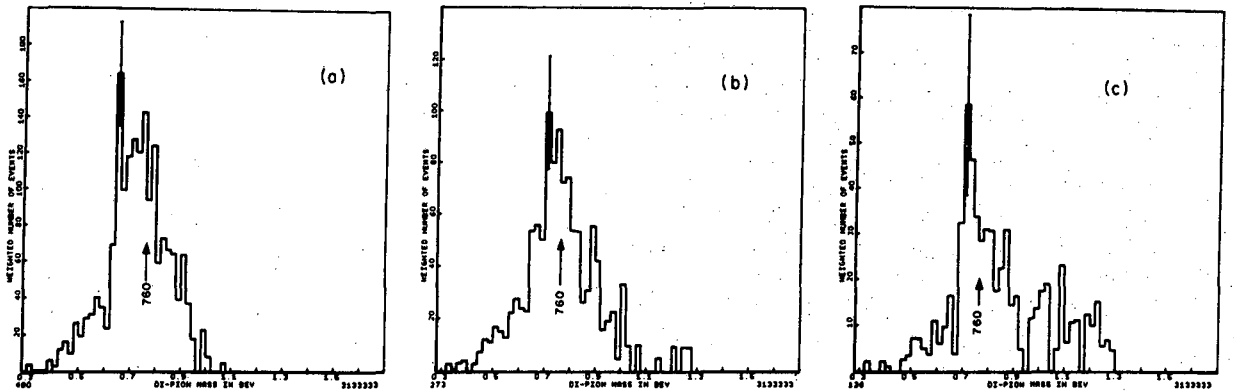The number 0.760 is a reference point indicating
the "accepted" ρ-mass value.
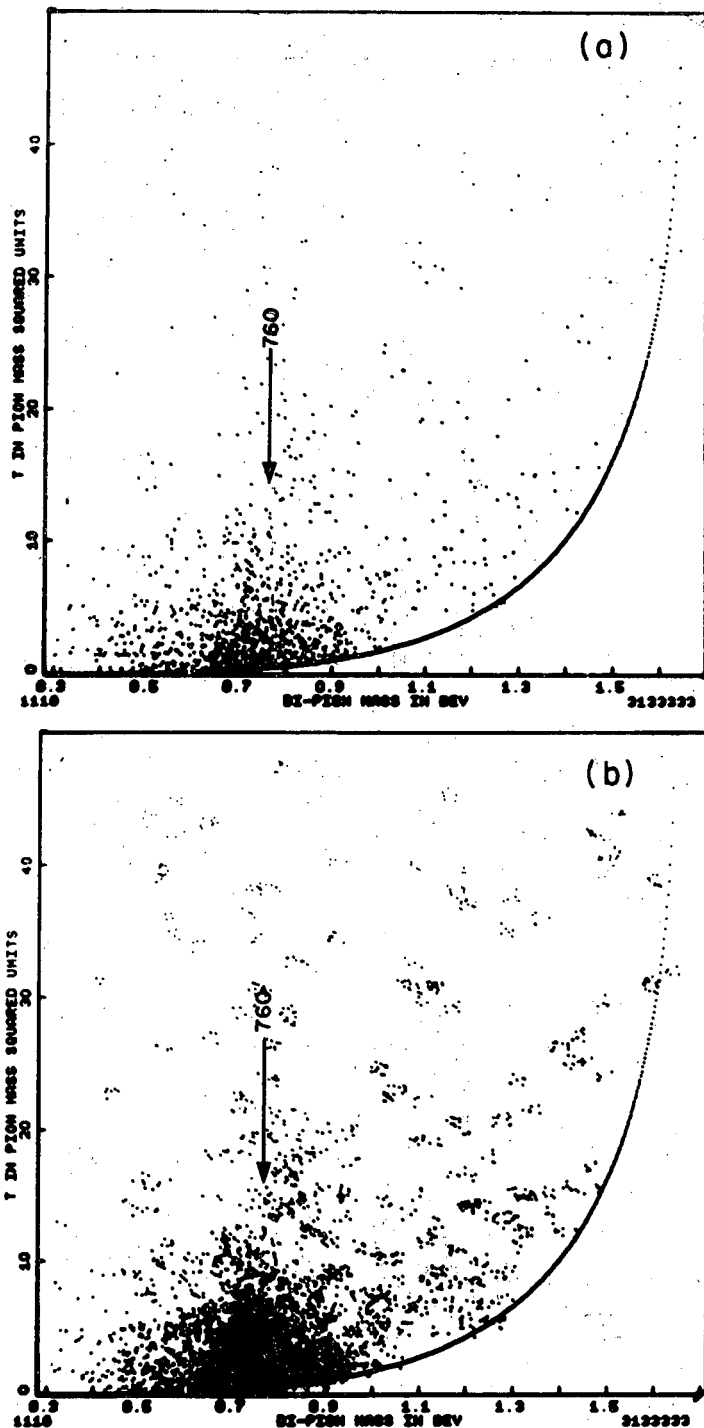
Fig. 15. Chew-Low plots $(\Delta^2 < 50 \ \mu^2)$:
(a) 3-BeV/c unweighted data
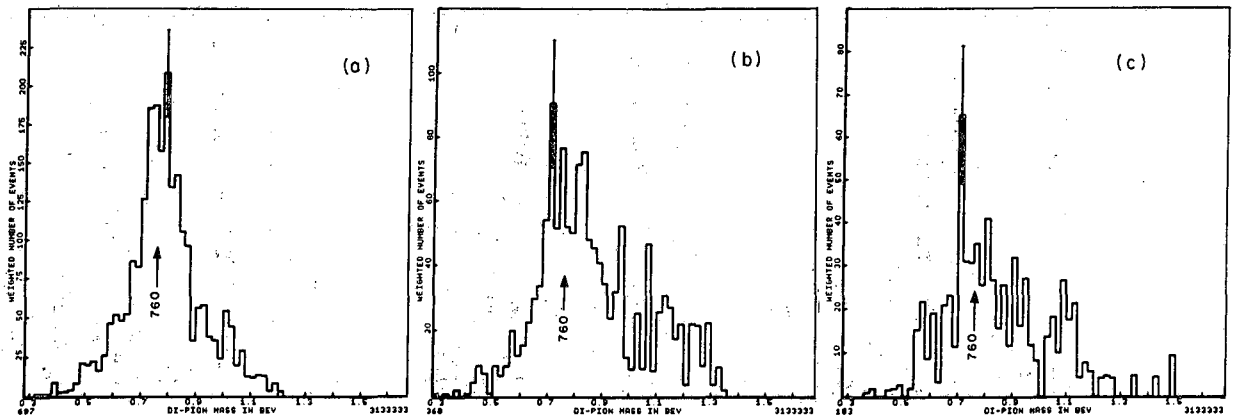(b) 3-BeV/c weighted data
See also caption for Fig. 14.
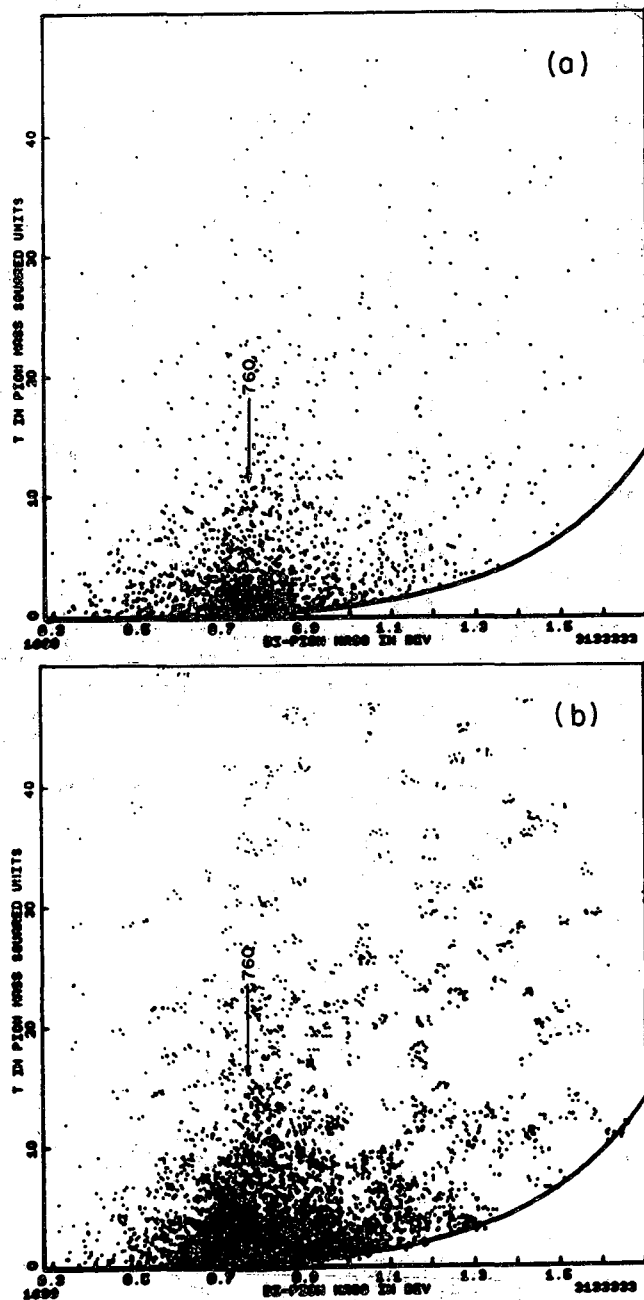
Fig. 16.   Chew-Low plots ($\Delta^2 < 50\ \mu^2$):
   (a) 4-BeV/c unweighted data
   (b) 4-BeV/c weighted data
   See also caption for Fig. 14.

Fig. 17. 3-BeV/c dipion weighted histograms:
(a) $\Delta^2 0 \rightarrow 3 \ \mu^2$
(b) $\Delta^2 3 \rightarrow 6 \ \mu^2$
(c) $\Delta^2 6 \rightarrow 9 \ \mu^2$
See also caption for Fig. 14.

Fig. 18. 4-BeV/c dipion weighted histograms:
   (a) $\Delta^2 0 \to 3 \; \mu^2$
   (b) $\Delta^2 3 \to 6 \; \mu^2$
   (c) $\Delta^2 6 \to 9 \; \mu^2$
   See also caption for Fig. 14.
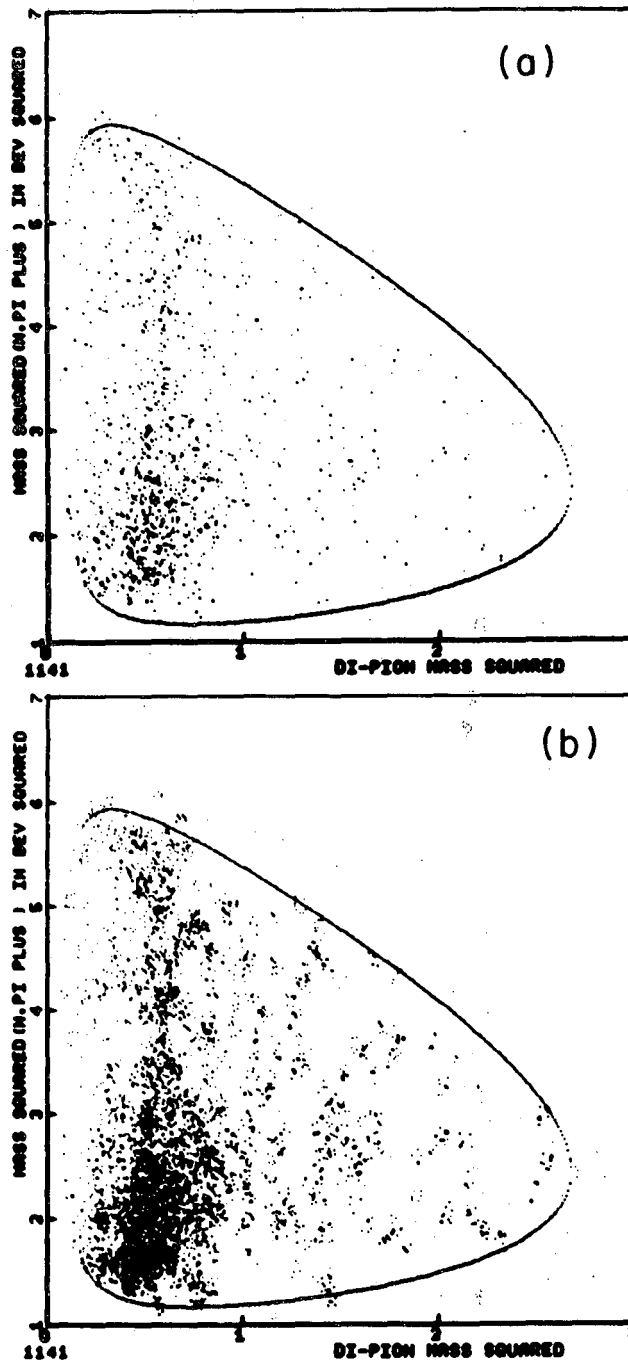
Fig. 19. $(M_{\pi^+ n})^2$ vs $M_{\pi\pi}^2$ all Δ^2 3 BeV/c:
(a) unweighted
(b) weighted.
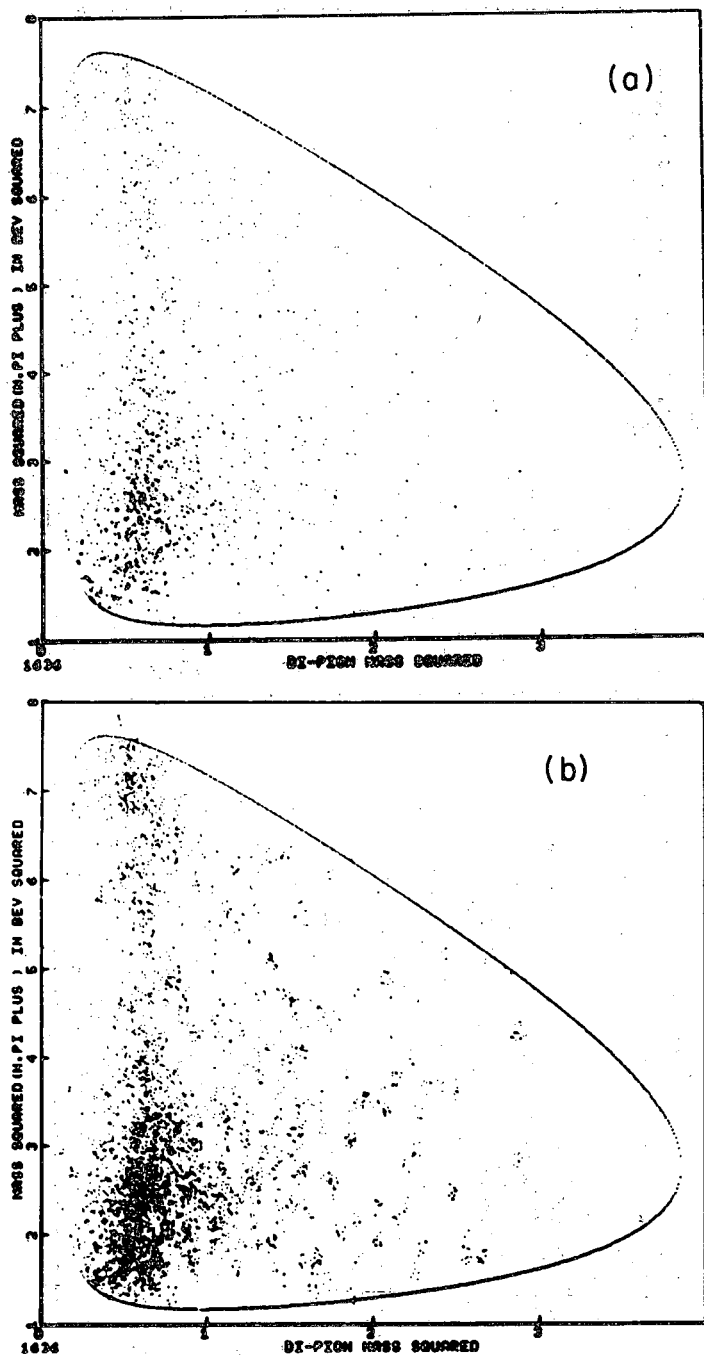
MUB-9971

Fig. 20. $(M_{\pi^+n})^2$ vs $M_{\pi\pi}^2$ all Δ^2 4 BeV/c:
(a) unweighted
(b) weighted.
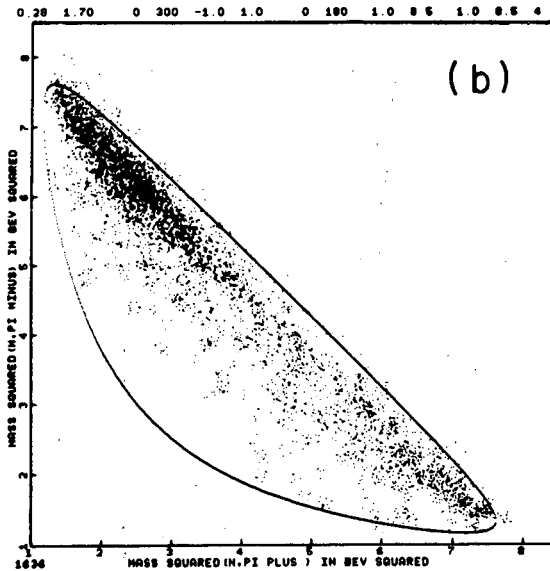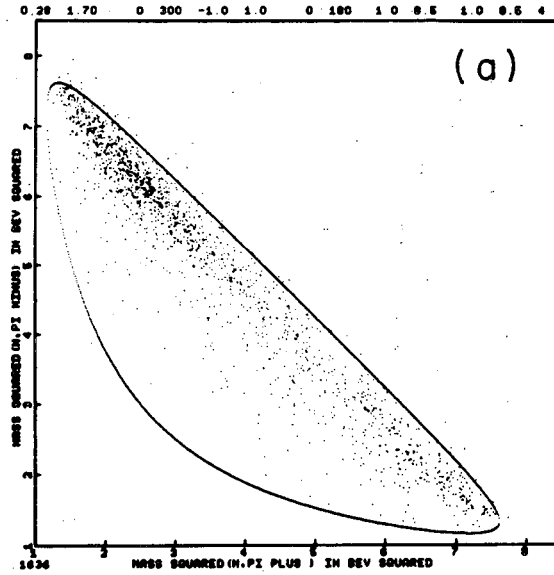
Fig. 21. $(M_{\pi^+ n})^2$ vs $(M_{\pi^- n})^2$ for all Δ^2 at 4 BeV/c:
(a) unweighted
(b) weighted.

MUB-9988

C. The ρ Region and Decay

The Δ^2 vs $\cos \theta_{\pi\pi}$ scatter plots in Figs. 22(a) and (b) (3 BeV/c), and 23(a) and (b) (4 BeV/c) show the well-known forward-backward asymmetry in $\cos \theta_{\pi\pi}$ at low values of Δ^2. However, in the larger Δ^2 regions the $\cos \theta_{\pi\pi}$ distribution does not appear to become uniform and thus differs from the data of Selove et al.[25] Again, the geometrical bias precludes a more quantitative and thus more meaningful comparison.

A similar set of plots for the Treiman-Yang angle vs Δ^2 is shown in Figs. 24 and 25. The approximately isotropic nature of the distribution apparent at low Δ^2 values again results from a strong OPE process. The problem with the OPE model is illustrated by the Δ^2 histograms shown in Fig. 26. For both 3 and 4 BeV/c, the ρ^0 production is much more peripheral than OPE, but can be fitted very well by OPE modified by either the Gottfried-Jackson absorption theory[9] (OPEA) or the Amaldi-Selleri[26] form factor. This form factor depends only on Δ^2 and does not include any correlations in the decay of the ρ that appear in the $\cos \theta_{\pi\pi}$ vs ϕ_{TY} plot ($M_{\pi\pi} = 600 \rightarrow 900$ MeV) shown in Figs. 27 and 28 for the 3 and 4 BeV/c data, respectively. The OPEA on the other hand does predict correlations stating that the decay distribution should be of the form

$$W(\theta,\phi) \propto \rho_{00} \cos^2 \theta + \rho_{11} \sin^2 \theta - \rho_{1,-1} \sin^2 \theta \cos 2\phi$$

$$- \sqrt{2} \, \text{Re} \, \rho_{10} \sin 2 \theta \cos \phi,$$

where ρ_{00}, ρ_{11}, $\rho_{1,-1}$ are real density matrix elements and ρ_{10} is complex ($\phi = \phi_{TY}$ and $\theta = \theta_{\pi\pi}$). (See Reference 9 for the details.)
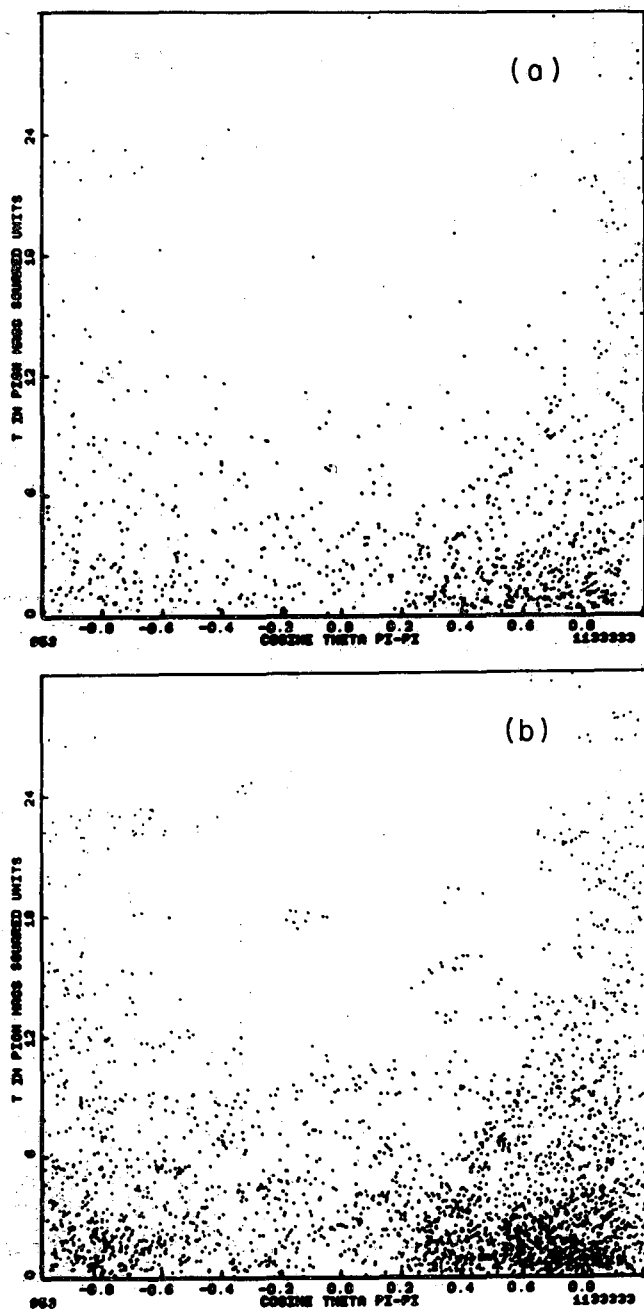
Even though this equation fits the charged ρ decay data very well, it does not predict any forward-backward asymmetry in $\cos \theta_{\pi\pi}$ or a large enhancement in the region ($\cos \theta_{\pi\pi} = 0 \rightarrow 0.5, \phi_{TY} = 120 \rightarrow 180$ deg), which is characteristic of the ρ^0 decay.

The possibility that an (I-spin = 0) s-wave interaction causes this structure led Durand and Chiu[2] to make a detailed calculation which included an s-wave resonance (called the ϵ^0) whose mass and width were comparable with those of the ρ. Their theory, which includes the Gottfried-Jackson absorption effects with no form factors, adds terms proportional to $\sin \theta \cos \phi$ and $\cos \theta$ to the distribution $W(\theta,\phi)$ mentioned before. Some bubble chamber ρ^0
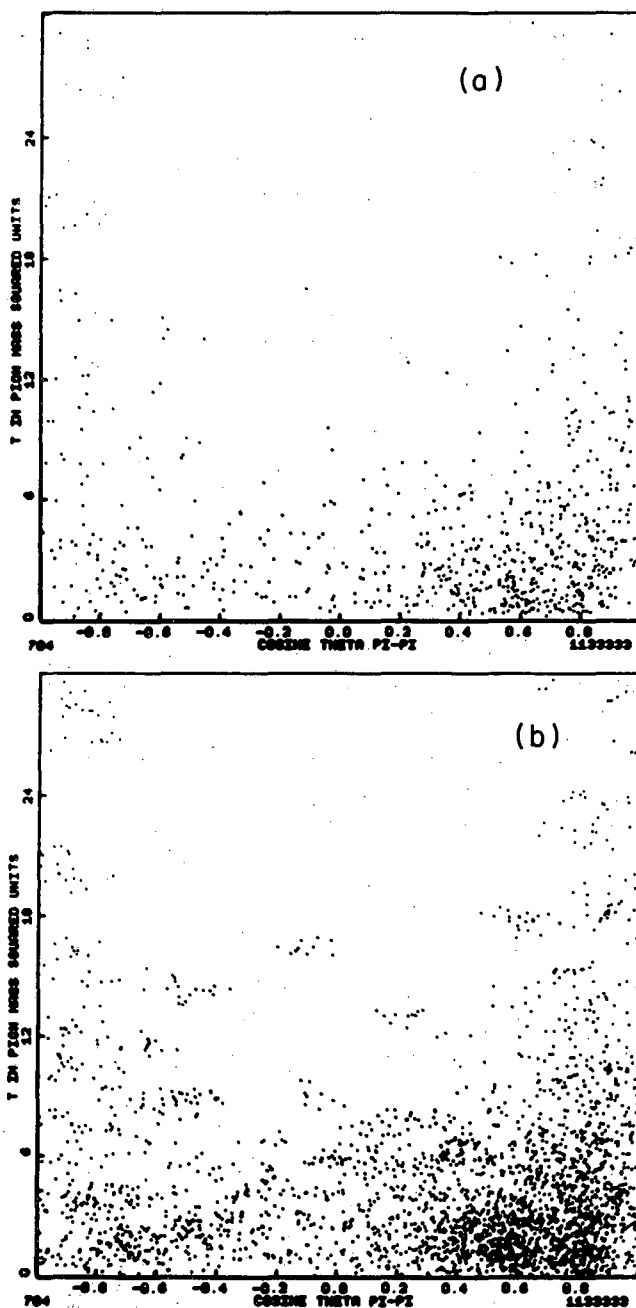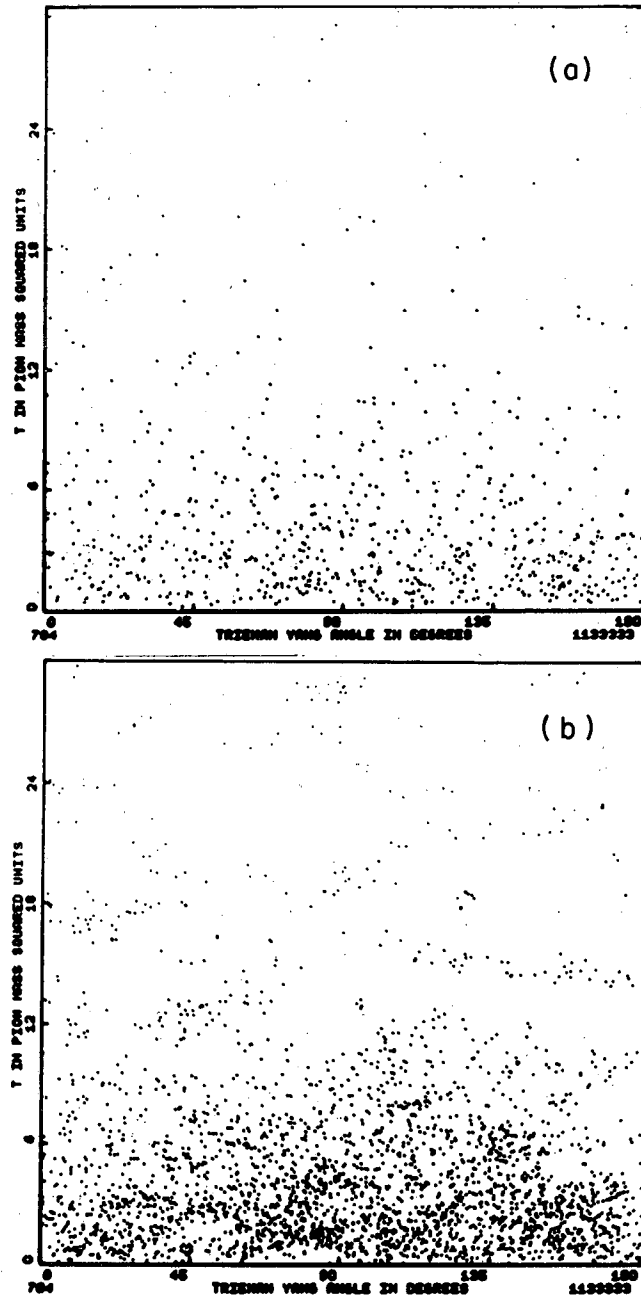
Fig. 22. Δ^2 vs $\cos\theta_{\pi\pi}$; ρ region ($M_{\pi\pi} = 0.6 \to 0.9$ BeV); 3 BeV/c:
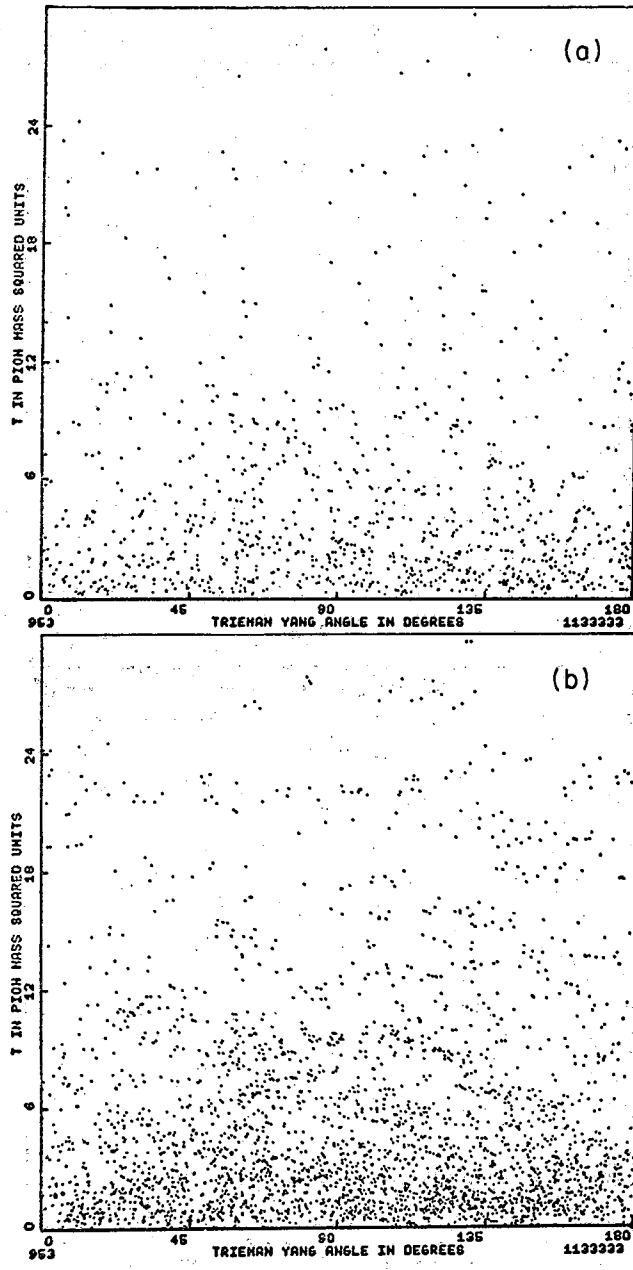   (a) unweighted
    (b) weighted.

Fig. 23. Δ^2 vs cos $\theta_{\pi\pi}$ ρ region, 4 BeV/c:
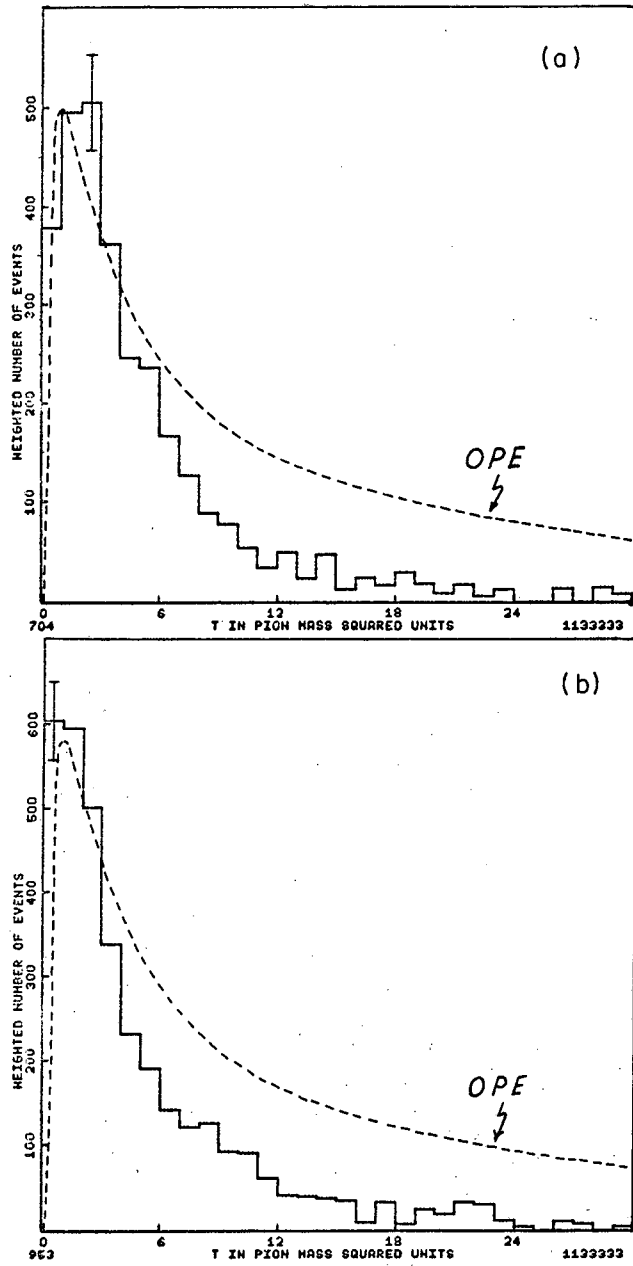   (a) unweighted
   (b) weighted.

Fig. 24. Δ^2 vs ϕ_{TY}, ρ region, 3 BeV/c:
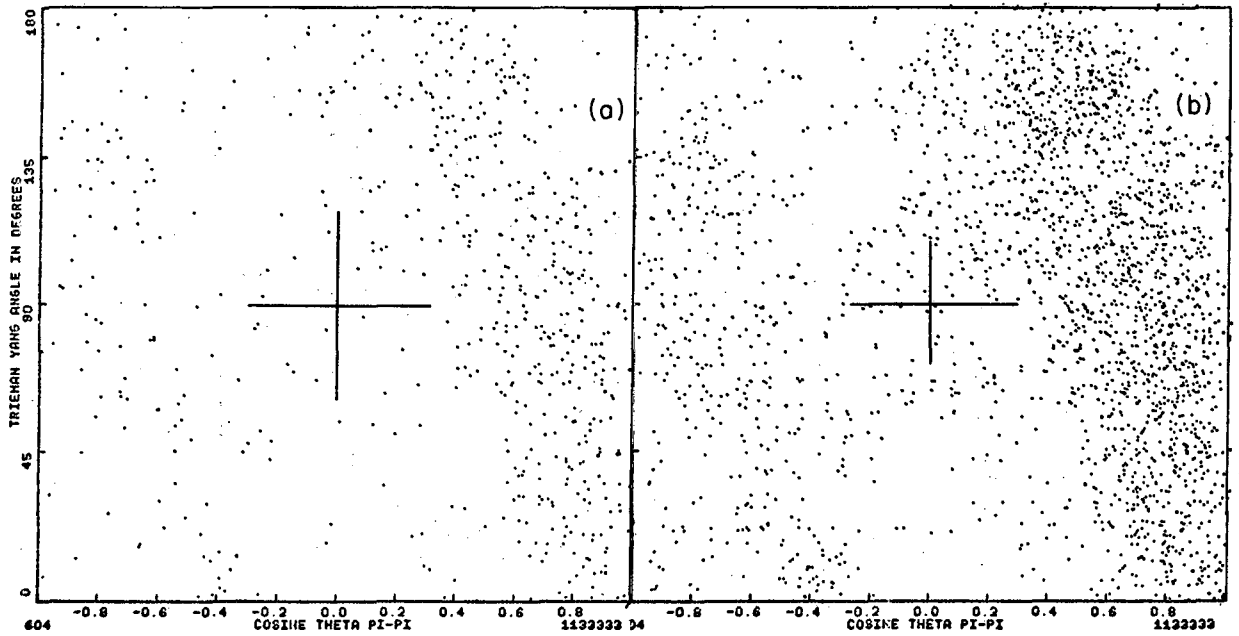(a) unweighted
(b) weighted.

Fig. 25. Δ^2 vs ϕ_{TY}, ρ region, 4 BeV/c:
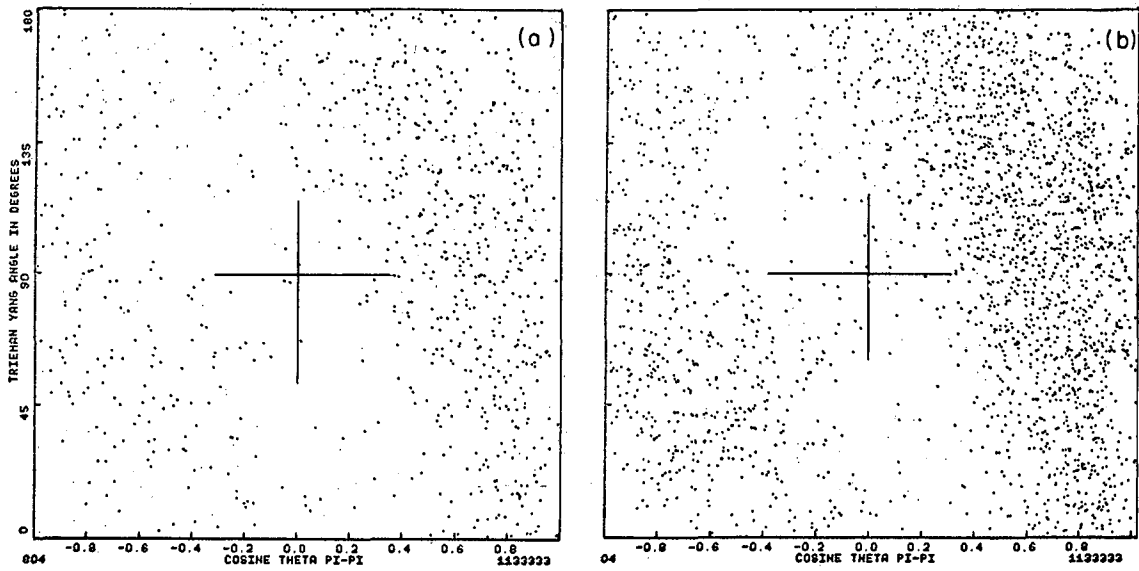(a) unweighted
(b) weighted

Fig. 26. Δ^2 weighted histogram showing unnormalized OPE curve:
(a) 3 BeV/c
(b) 4 BeV/c.

Fig. 27. ϕ_{TY} vs $\cos\theta_{\pi\pi}$ for $\Delta^2 < 9\,\mu^2$ in the ρ region 3 BeV/c:
(a) unweighted
(b) weighted

MUB-9966

Fig. 28. ϕ_{TY} vs cos $\theta_{\pi\pi}$ for $\Delta^2 < 9 \mu^2$ in the ρ region 4 BeV/c:
(a) unweighted
(b) weighted

data fits this theory very well when the following parameters are assumed:[27]

    1. Mass of e^0 = 0.730 BeV,

    2. Width of ϵ^0 = 0.090 BeV,

    3. ϵ^0/ρ^0 production ratio = 0.15 .

The results of the Durand and Chiu calculation are shown in Fig. 29 for 3 BeV/c. The curves are lines of constant probability as predicted by the model for $\Delta^2 < 10 \ \mu^2$, averaged over the mass interval 700 MeV < $M_{\pi\pi}$ < 800 MeV. (The 4-BeV/c calculation is similar but not shown. See Reference 27.) The data in Figs. 27 and 28 certainly agree qualitatively but a direct numerical fitting has not been attempted due to the difficulties introduced by the geometrical bias.

If such a theory is more than conjecture, one would expect to see some evidence of this ϵ^0 in a mass plot. Feldman et al.[28] have seen evidence for a $\pi^0\pi^0$ resonance near 720 MeV, but a definite interpretation of this as the ϵ^0 has not yet been given.

One method of looking at the correlations in $M_{\pi\pi}$, Δ^2, $\cos\theta_{\pi\pi}$, and ϕ_{TY} is by a kind of "four-dimension" plot. The 3-BeV/c data shown in Fig. 30 (a through ℓ) are really 12 separate unweighted Chew-Low plots, each for a particular $\cos\theta_{\pi\pi}$ - ϕ_{TY} region. Note that the center of gravity of the dipion mass in the ρ region (0.6 → 0.9 BeV) is not in the same place for all regions. In particular, there is a significant shift from $\approx$ 780 to $\approx$ 700 MeV in going from regions j to ℓ ($\cos\theta_{\pi\pi}$ = 0.5 → 1.0; ϕ_{TY} = 0° → 60° to ϕ_{TY} = 120° → 18-°). There is also a similar though statistically weak shift in going from regions c to a. Region i shows a center of gravity of $\approx$ 700 MeV; it is interesting to note that this region is heavily populated for ρ^0 decay, but not for $\rho^{\pm}$.

These effects are even more striking in the corresponding Fig. 31 (a through ℓ) for 4 BeV/c. Some possible consequences of this are discussed in Section V.

Figure 32(a) is a histogram of the combined (3 and 4 BeV/c) unweighted data for all regions of the plots in Figs. 30 and 31 except a, i, and ℓ. Note that the ρ peak at $\approx$ 760 MeV has a width of $\approx$ 180 MeV. The regions a, i, and ℓ [Fig. 32(b)] show the dipion mass peak at $\approx$ 700 MeV. Note also that the number of events below 600 MeV is greater for Fig. 32(b) than for Fig. 32(a). I originally thought that the geometrical bias might play a role
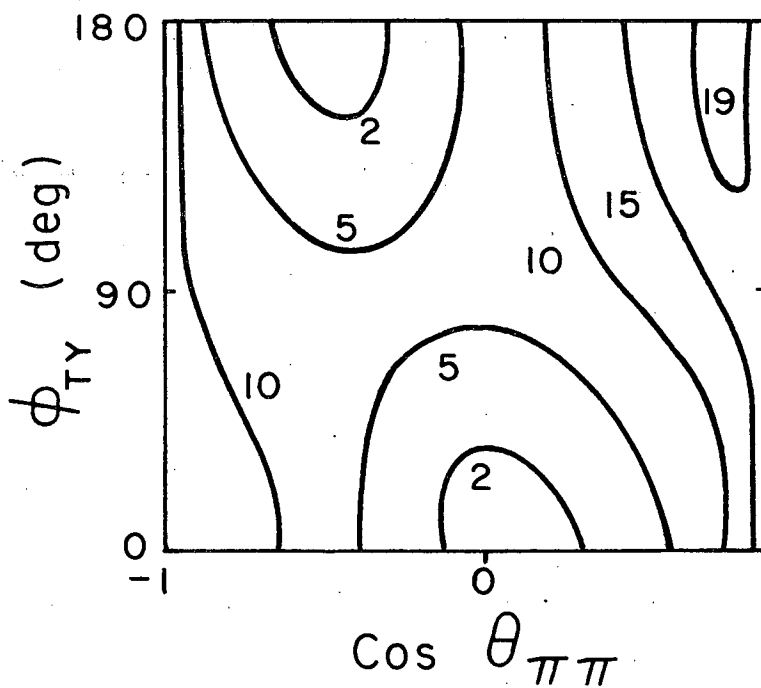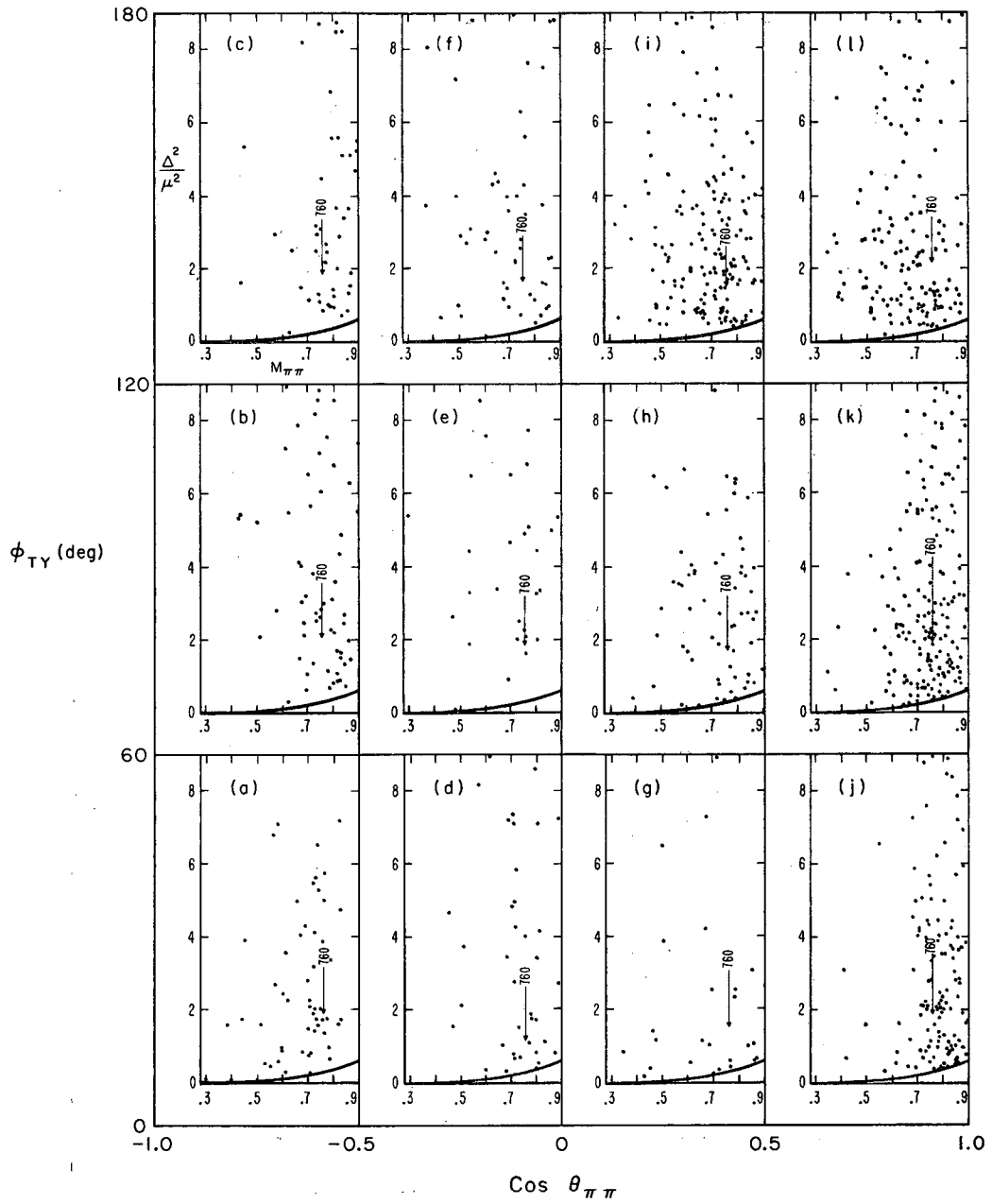
MUB-9984

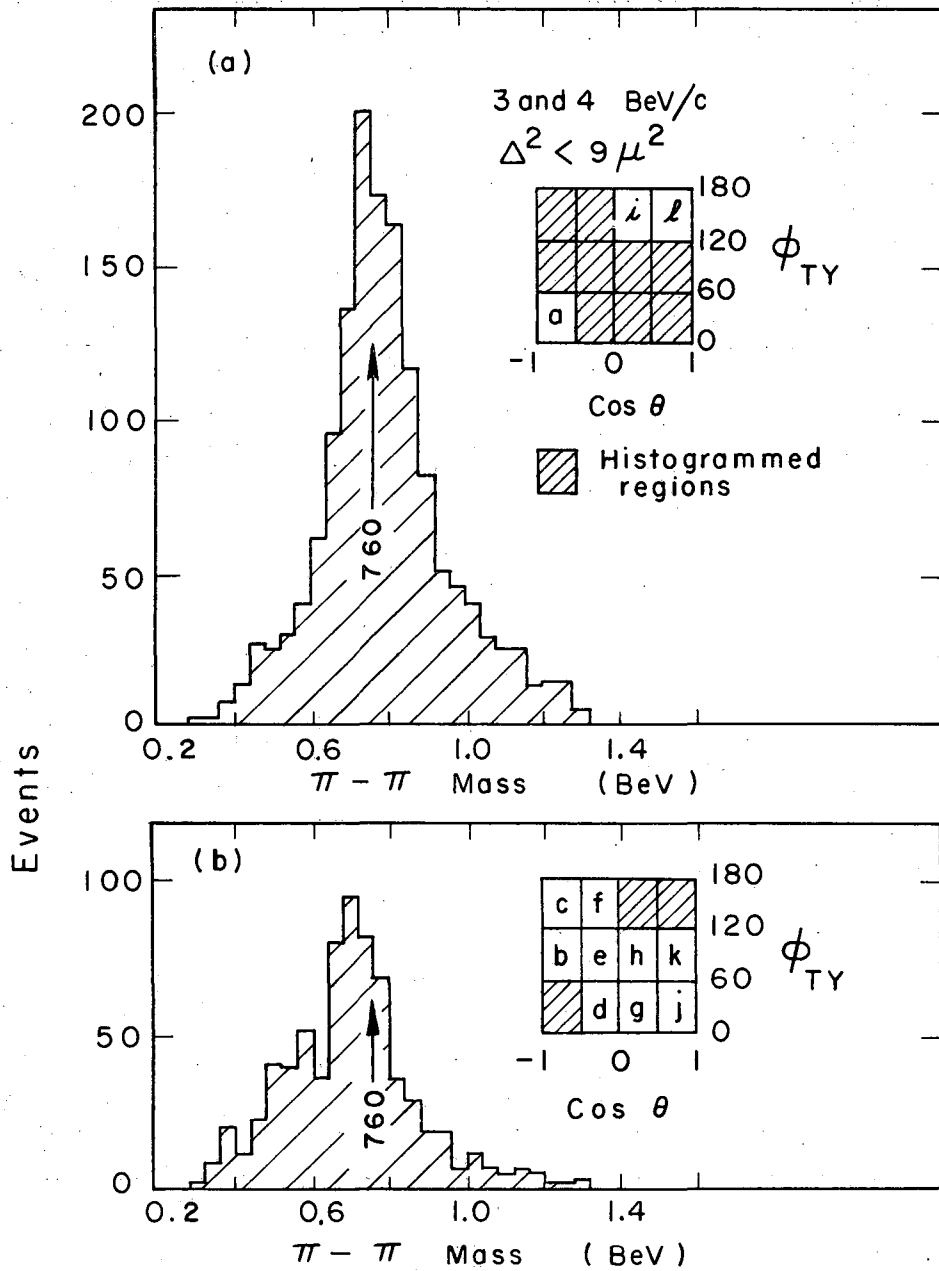Fig. 29. Theoretical calculation of Durand and Chiu
     model for 3 BeV/c.
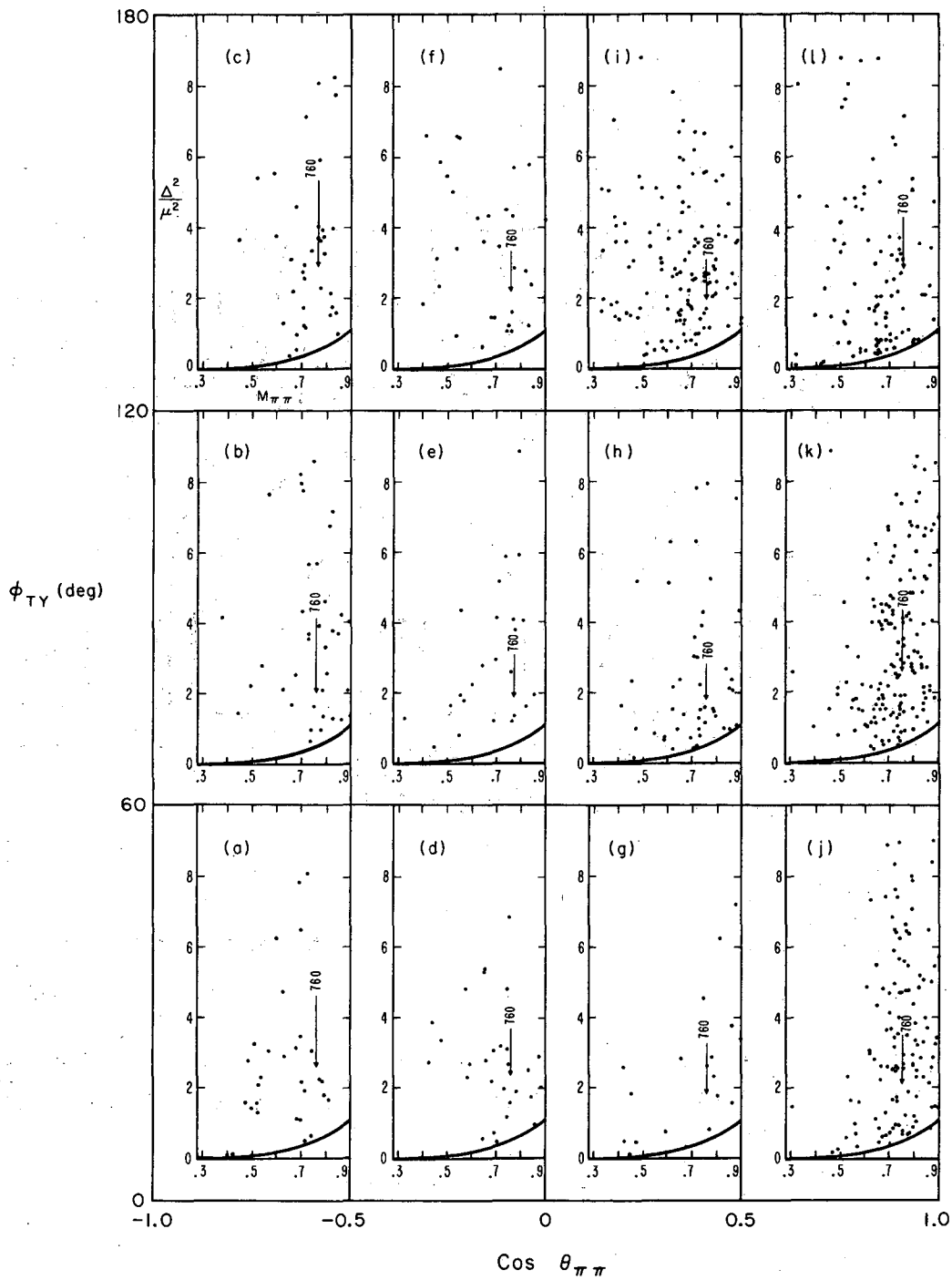
Fig. 30.   Chew-Low plots 3 BeV/c $\Delta^2 < 9\,\mu^2$.

MUB-10090

Fig. 31. Chew-Low plots 4 BeV/c $\Delta^2 < 9\,\mu^2$.
The curves are the kinematical boundaries.

MUB-10089

Fig. 32. Histograms of regions a, i, and ℓ vs other regions.
(a) 3 and 4 BeV/c, all regions except a, i, and ℓ.
(b) 3 and 4 BeV/c, regions a, i, and ℓ.

MUB-9983

in this shifting, but Monte-Carlo calculations showed that the bias could not cause such a shift.

If the ϵ^0 were s-wave it might be seen near 90° ($\cos \theta_{\pi\pi}$ = 0) in the dipion scattering angle where the ρ influence is minimal because of the strong $\cos^2 \theta_{\pi\pi}$ decay dependence. Figure 33 shows the dipion mass spectra for outside (upper histogram) and inside (lower) a (-0.3 to +0.3) region in $\cos \theta_{\pi\pi}$ (including all ϕ_{TY}). A comparison of the two histograms in the ρ region does not show the significant mass-peak shift that was reported by Selove et al.[29]
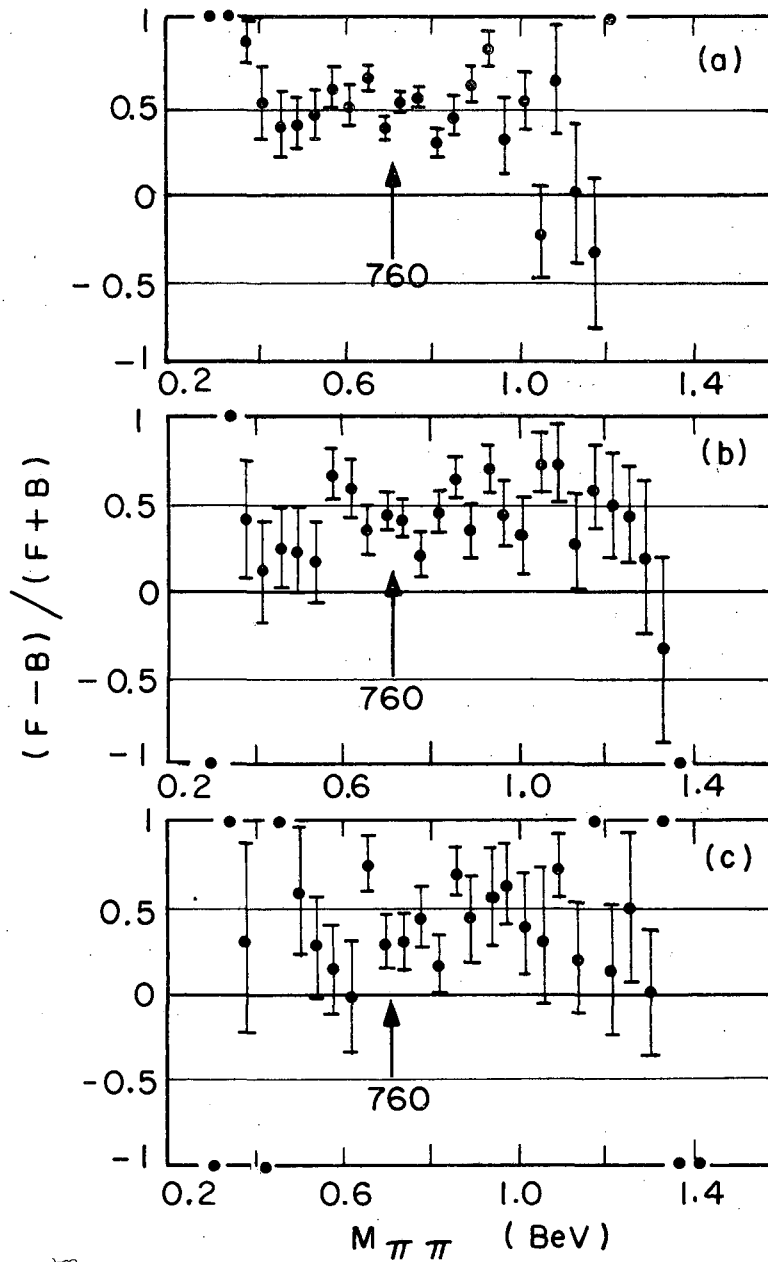
Figure 34 shows the (F-B)/(F+B) ratio for the combined data as a function of $M_{\pi\pi}$ for three low Δ^2 regions ($0 \to 3\,\mu^2$, $3 \to 6\,\mu^2$, $6 \to 9\,\mu^2$). In the ρ region, the ratio is ≈ 0.5 for the lowest Δ^2 region and ≈ 0.3 for the highest Δ^2 region.[30]
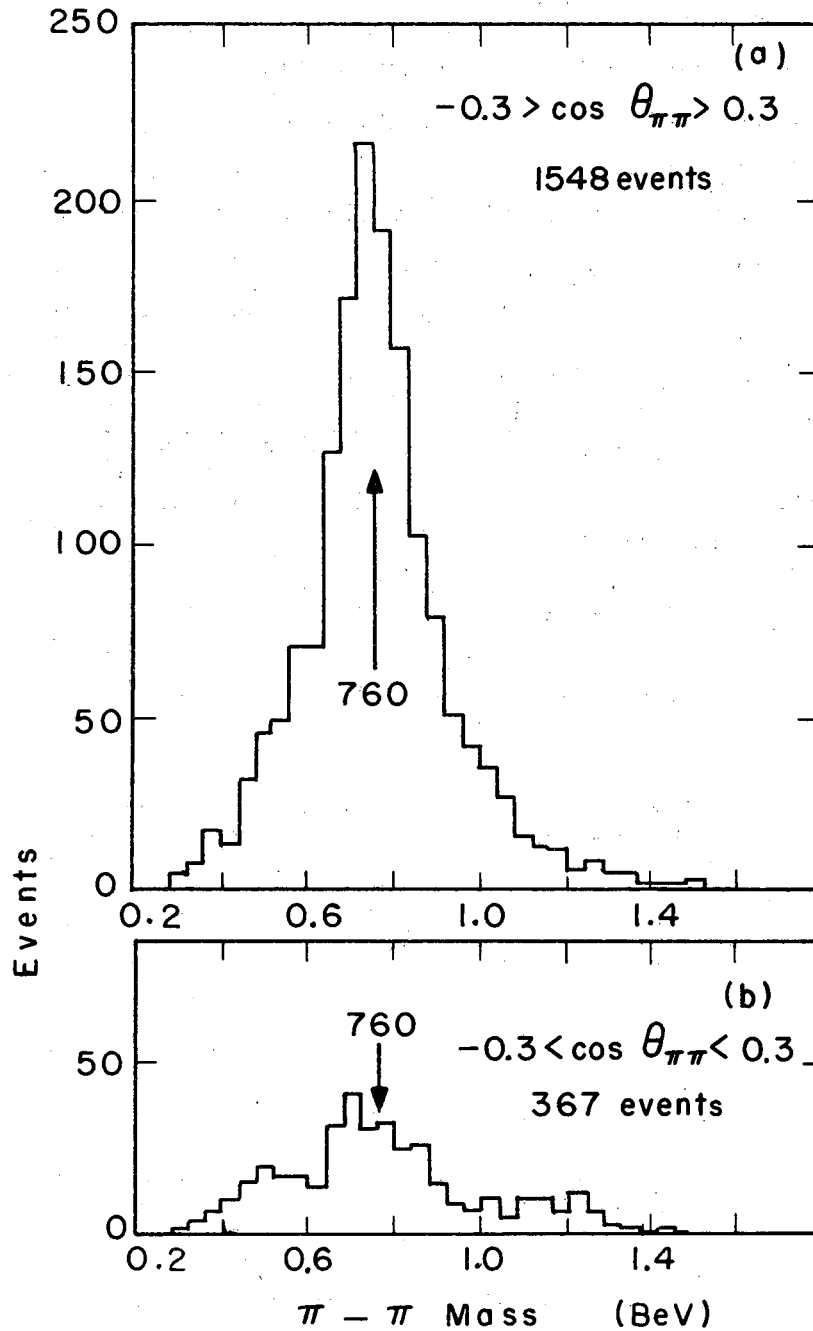
Fig. 33. Dipion histogram for $\Delta^2 < 9\,\mu^2$, $\cos\theta_{\pi\pi} = -0.3$ to $+0.3$, and 3 and 4 BeV/c,
  (a) outside the -0.3 to 0.3 region
  (b) inside the -0.3 to 0.3 region.

Fig. 34. (F-B)/(F+B) 3 and 4 BeV/c,
(a) $\Delta^2 < 3\ \mu^2$
(b) $\Delta^2\ 3 \rightarrow 6\ \mu^2$
(c) $\Delta^2\ 6 \rightarrow 9\ \mu^2$

MUB-9982

V. CONCLUSIONS

The most striking results of this experiment are the mass-peak shifts in the dipion spectra for different regions of $\cos\theta_{\pi\pi}$ and ϕ_{TY} (shown in Figs. 30 and 31). The data of regions i ($\cos\theta_{\pi\pi} = 0 \to 0.5$; $\phi_{TY} = 120 \to 180°$) and ℓ ($\cos\theta_{\pi\pi} = 0.5 \to 1$; $\phi_{TY} = 120° \to 180°$) show a peak in the dipion mass spectrum near 700 MeV. One is tempted to state that this is a confirmation of the Durand and Chiu theory[2] because the maximum intensity of the ϵ^0 interference occurs in those regions. However, the formulas for the decay distribution are _averaged_ over the ρ mass interval. To compare any mass shifting with theory, one would need to know the mass dependence of the terms of the decay distribution (more specifically, the density-matrix elements).

The absorptive aspects (non-OPE) in the theory cause the Treiman-Yang correlations. The ϵ^0 - ρ^0 interference both being produced by OPE can _not_ cause any such correlations. Thus the previously mentioned mass shifting _could_ be due simply to non-OPE porcesses. It would be interesting and also important to see if the Durand and Chiu theory or a similar one could cause the mass shifts observed in our experiment.

Our experiment also points out the utility of the spark chamber technique for accurate measurements with high statistics in specific regions of phase space. Even though we had anticipated more events and greater accuracy, the principle is good and a number of the features are being incorporated in another experiment which should be much more accurate and obtain a 100-fold increase of data.

I have not yet said anything about the $\omega \to 2\pi$ decay. It is certainly possible that the ρ-ω interference effects exist but no statistically significant one was seen. The shift of the ρ^0 with Δ^2 could be partly explained by the different Δ^2 dependence of the $\omega \to 2\pi$, but it is also possible that a particle such as the ϵ^0 would have a stronger contribution at very low Δ^2. The $(F-B/(F+B)$ ratio being largest at low Δ^2 could be a consequence of this contribution.

Because the question of the existence of this ϵ^0 and the $\omega \to 2\pi$ decay is still far from settled, it is desirable to increase the statistics and push the dipion mass accuracy down to a few MeV. A spark chamber spectrometer system with good optics can readily accomplish this, with similar analysis techniques being used.

I would like also to discuss a preliminary report in which some 4 BeV/c π^- data of this experiment were used.[31] The preliminary results showed a double enhancement in an unconstrained dipion mass plot for $\Delta^2 < 9\,\mu^2$. The histograms of Fig. 14 are clearly different, for the following reasons:

(a) The preliminary results were partly in error due to a computer program bug which reversed the correction for the stray magnetic field between the A and T chambers. Consider an event produced with a dipion mass near 750 MeV. The opening angle is $\approx 23°$ for low Δ^2. Figure 35 shows schematically an AT, AT event. The trajectories are bent either away from or towards each other, depending on the orientation of the particles with respect to the magnetic field. A reversed stray-field correction will cause the analysis programs to calculate a higher mass for one and a lower for the other. (The change in dipion mass varied from 5 to 15 MeV.)

(b) The variable Δ^2 has a kinematically constrained lower limit that is near but greater than zero for dipion masses near the ρ region. The statistical errors permit a value of $\Delta^2 < 0$ before constraining. For the preliminary data presented at Dubna,[31] these events were erroneously left out of the mass plot.

(c) Events with trajectories that passed through the S chamber were calculated incorrectly because the chamber was not aligned properly. (Alignment was difficult because no straight-throughs were bent enough by the Sagane magnet to go through the S or C chamber. The alignment was effected by comparing the M chamber's impact parameter with the S impact parameter for many events.)

A final remark: The dipion mass peak in the ρ region shifts with (a) Δ^2 and (b) the $\cos\theta_{\pi\pi}$ and ϕ_{TY} region for both beam energies. This agreement makes the results and conclusions more reliable (and thus more meaningful) because the geometrical bias imposed upon the final-state particles differs for the two energies.

)
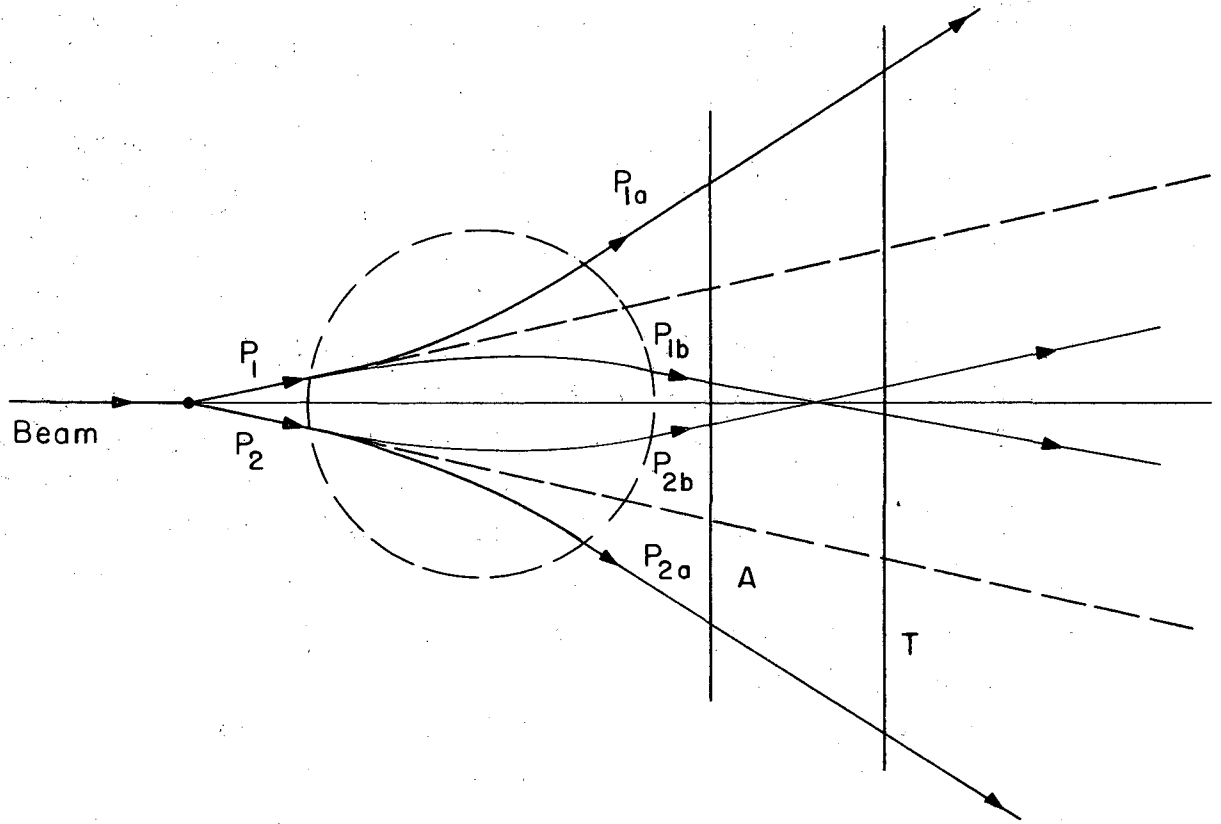
MUB-9980

Fig. 35. Schematic showing possible event trajectories for
      an AT-AT event:
      (a) Sagane magnet B_z upward
      (b) Sagane magnet B_z downward
      Dashed denotes the approximate Sagane magnetic field region.

ACKNOWLEDGMENTS

APPENDIX: WEIGHTED HISTOGRAM AND ITS STATISTICAL ERROR

Given n observed events in a certain "small" region of phase space. All n of these events have the same detection probability p because they are "identical" in the sense that the region of phase space is "small". If the experimental apparatus could detect all of the events in this region $N = n/p$ would be expected.

If we assume that $\sigma_n = \sqrt{n}$ (σ = statistical standard deviation) and that p is known well enough to be considered "errorless" ($\delta p/p \ll \frac{\sqrt{n}}{n}$), then $\sigma_N = (1/p) \sigma_n = (1/p)\sqrt{n}$ (note this is greater than $\sqrt{N}$). Define w as $1/p$, the weight for these events ≥ 1.

Consider a larger region of phase space which includes the following:

$$n_1, w_1; n_2, w_2; \cdots ; n_j, w_j \quad \text{all independent.}$$

Consider the sum

$$S = w_1 n_1 + w_2 n_2 + \cdots + w_j n_j;$$

then

$$\sigma_S = \left[w_1^2 \sigma_{n_1}^2 + w_2^2 \sigma_{n_2}^2 + \cdots + w_j^2 \sigma_{n_j}^2 \right]^{\frac{1}{2}}.$$

Now let $n_1 = n_2 = \cdots = n_j = 1$;

then

$$\sigma_S = \left[w_1^2 + w_2^2 + \cdots + w_j^2 \right]^{\frac{1}{2}}.$$

S can be considered a bin in a weighted histogram and σ_S the statistical error.

FOOTNOTES AND REFERENCES

1. D. Keefe, L. T. Kerth, C. M. Noble, J. J. Thresher, and W. A. Wenzel, A Magnetic Spectrometer Using Spark Chambers to Obtain Large Solid Angle and High Resolution in π-π Interaction Studies, Nucl. Instr. Meth. 20, 171-172 (1963).

2. L. Durand and Y. T Chiu, Phys. Rev. Letters 14, 329, 680(E), (1965).

3. For an excellent historical review, see the introduction of A Study of Di-Pion Resonances Produced at Low Momentum Transfer in $\pi^- + p \rightarrow \pi^- + \pi^+ + n$ at 1.6 BeV/c (Ph. D. Thesis) by Alan R. Clark, Princeton University (August 1964). See also W. Selove, Rev. Mod. Phys. 37, 460 (1965).

4. V. Hagopian (Ph. D. Thesis), The Reaction $\pi^- + p \rightarrow \pi + \pi +$ nucleon at 3 BeV/c, University of Pennsylvania (1963).

5. Aachen-Berlin-Birmingham-Bonn-Hamburg-London-München Collaboration, Nuovo Cimento 31, 729 (1964).

6. Saclay-Orsay-Bari-Bologna Collaboration, Nuovo Cimento 35, 713 (1965).

7. A. Rosenfeld, Angela Barbaro-Galtieri, W. H. Barkas, Pierre L. Bastien, Janos Kirz, and Matts Roos, Rev. Mod. Phys. 37, 633 (1965).

8. B. Sechi Zorn, Phys. Rev. Letters 8, 282 (1962).

9. K. Gottfried and J. D. Jackson, Nuovo Cimento 34, 735 (1964). See also J. D. Jackson, Rev. Mod. Phys. 37, 484 (1965).

10. S. B. Treiman and C. N. Yang, Phys. Rev. Letters 8, 140 (1962).

11. D. I. Meyer and K. M. Terwilliger, in Proceedings of an International Conference on Instrumentation for High-Energy Physics (Interscience Publishers, New York, 1961), p. 276.

12. The same high-voltage electronics has been used in the following:
    (a) William R. Holley, K^--Proton Elastic Scattering in the Momentum Range 700 to 1400 BeV/c, (Ph. D. Thesis), UCRL-16274, October 1965 (unpublished); (b) Richard L. Crolius, A Measurement of the Polarization of Sigma-Zero Hyperons Produced by Pi-Minus Mesons on Hydrogen near 1.3 BeV/c, (Ph. D. Thesis), UCRL-16089, May 1965 (unpublished).

13. J. C. Hodges, D. Keefe, L. T. Kerth, J. J. Thresher, and W. A. Wenzel, Digitized Measuring Projector for the Analysis of Spark-Chamber Photographs, UCRL-10251 (May 1962).

14. The Magnetic Measurements Group under Peter Watson at the Lawrence
    Radiation Laboratory now has many sophisticated methods of measur-
    ing magnetic fields which are outgrowths of the simple flip coil used
    for the measurements in this experiment.

15. A. H. Rosenfeld and James N. Snyder, Digital-Computer Analysis of
    Data from Bubble Chambers, UCRL-9098 (February 1960).

16. C. Noble, Match 2 (1964), LRL internal report (unpublished).

17. L. Meissner, Orbit 3, LRL Computer Center internal report (unpublished).

18. F. Solmitz, Ann. Rev. Nucl. Sci. 14, 375 (1964).

19. P. Berge, Alvarez Group Physics Notes 86, Lawrence Radiation
    Laboratory (1962) (unpublished).

20. W. A. Wenzel, Probability for Detecting a Di-Pion Event, LRL internal
    report BeV-881.

21. Gerald R. Lynch, Program FAKE: Monte Carlo Simulation of Bubble
    Chamber Events, UCRL-10335 (July 1962).

22. W. Selove, V. Hagopian, H. Brody, A. Baker, and E. Leboy,
    Phys. Rev. Letters 9, 272 (1962).

23. Richard Lander (University of California, San Diego), private com-
    munication, 1964.

24. A. S. Goldhaber, Phys. Rev. 134, B600 (1964).

25. See Reference 3 and V. Hagopian, W. Selove, J. Alitti, J. P. Baton,
    M. Neveu-Rene, R. Gessaroli, A. Romano, Phys. Rev. Letters 14,
    1077 (1965).

26. U. Amaldi and F. Selleri, Nuovo Cimento 31, 360 (1964).

27. I. Derado, V. P. Kenney, J. A. Poirer, W. D. Shephard, Phys. Rev.
    Letters 14, 872 (1965).

28. M. Feldman, W. Frati, J. Halpern, A. Kanofsky, M. Nussbaum,
    S. Richert, P. Yamin, A. Choudry, S. Devons, J. Grunhaus,
    Evidence for a New 2π Resonance at 700 MeV, Phys. Rev. Letters
    14, 869 (1965).

29. The shift seen in Reference 22 was very marginal statistically.

30. This agrees with data soon to be published by Larry Jacobs (Ph. D. thesis
    in preparation), Lawrence Radiation Laboratory, private communica-
    tion.

31. D. Keefe, L. T. Kerth, C. M. Noble, J. J. Thresher, W. A. Wenzel,
    Di-Pion Mass Spectrum from π⁻p Collisions at 4 BeV/c, UCRL-11468
    (July 1964).